

High-resolution simulations of the plume dynamics in an idealized 79°N Glacier cavity using adaptive vertical coordinates

Markus Reinert¹, Marvin Lorenz¹, Knut Klingbeil², Bjarne Büchmann³, and Hans Buchard¹

¹Leibniz Institute for Baltic Sea Research Warnemünde

²Leibniz Institute for Baltic Sea Research Warnemuende (IOW)

³Joint GEOMETOC Support Center

March 26, 2023

Abstract

For better projections of sea level rise, two things are needed: an improved understanding of the contributing processes and their accurate representation in climate models. A major process is basal melting of ice shelves and glacier tongues by the ocean, which reduces ice sheet stability and increases ice discharge into the ocean. We study marine melting of Greenland’s largest floating ice tongue, the 79° North Glacier, using a high-resolution, 2D-vertical ocean model. While our fjord model is idealized, the results agree with observations of the melt rate and the overturning strength. Our setup is the first application of adaptive vertical coordinates to an ice cavity. Their stratification-zooming allows a vertical resolution finer than 1 m in the entrainment layer of the meltwater plume, which is important for the plume development. In a sensitivity study, we show that the buoyant plume at the ice–ocean interface is responsible for the bulk of basal melting. The melting almost stops when the plume has reached neutral buoyancy. There, the plume detaches from the ice tongue and transports meltwater out of the fjord. The detachment depth depends primarily on the ambient ocean stratification. Our results contribute to the understanding of ice–ocean interactions in glacier cavities. Furthermore, we suggest that our modeling approach with stratification-zooming coordinates will improve the representation of these interactions in global ocean models. Finally, our idealized model topography and forcing are close to a real fjord and completely defined analytically, making the setup an interesting reference case for future model developments.

High-resolution simulations of the plume dynamics in an idealized 79°N Glacier cavity using adaptive vertical coordinates

Markus Reinert¹, Marvin Lorenz¹, Knut Klingbeil¹, Bjarne Büchmann²,
Hans Burchard¹

¹Leibniz Institute for Baltic Sea Research Warnemünde, Seestr. 15, 18119 Rostock, Germany

²Joint GEOMETOC Support Center, Danish Defence Acquisition and Logistics Organization (DALO),
Lautrupbjerg 1-5, 2750 Ballerup, Denmark

Key Points:

- Melting of the 79°N Glacier ice tongue by turbulent ocean currents is studied with an idealized 2D-vertical fjord model
- The role of the meltwater plume as the driver of basal melting is examined together with the influence of environmental factors
- A high vertical resolution finer than 1 m is achieved in the plume by the use of adaptive vertical coordinates that zoom to stratification

Abstract

For better projections of sea level rise, two things are needed: an improved understanding of the contributing processes and their accurate representation in climate models. A major process is basal melting of ice shelves and glacier tongues by the ocean, which reduces ice sheet stability and increases ice discharge into the ocean. We study marine melting of Greenland’s largest floating ice tongue, the 79° North Glacier, using a high-resolution, 2D-vertical ocean model. While our fjord model is idealized, the results agree with observations of the melt rate and the overturning strength. Our setup is the first application of adaptive vertical coordinates to an ice cavity. Their stratification-zooming allows a vertical resolution finer than 1 m in the entrainment layer of the meltwater plume, which is important for the plume development. In a sensitivity study, we show that the buoyant plume at the ice–ocean interface is responsible for the bulk of basal melting. The melting almost stops when the plume has reached neutral buoyancy. There, the plume detaches from the ice tongue and transports meltwater out of the fjord. The detachment depth depends primarily on the ambient ocean stratification. Our results contribute to the understanding of ice–ocean interactions in glacier cavities. Furthermore, we suggest that our modeling approach with stratification-zooming coordinates will improve the representation of these interactions in global ocean models. Finally, our idealized model topography and forcing are close to a real fjord and completely defined analytically, making the setup an interesting reference case for future model developments.

Plain Language Summary

The global increase of sea levels is a consequence of human-induced climate change. It presents a threat to coastal regions and demands action to protect human life and infrastructure near the coast. Planning protective measures requires projections of sea level rise, computed with climate models. We present an approach to improve the simulation of an important contributor to sea level rise: melting of floating ice shelves by ocean circulation. Our modeling approach uses a vertical model grid that evolves over time. The temporal evolution depends on the density structure of the ocean. Large density differences appear just below an ice shelf, where fresh meltwater mixes with salty seawater. The adaptive grid of our model resolves this mixing process in great detail. This is important for an accurate computation of the melt rate and enables us to study in depth the ice shelf–ocean interactions. We study them at the glacier tongue of the 79° North Glacier, which is Greenland’s largest ice shelf. The physical understanding gained from our simulations is also applicable to other floating glacier tongues and ice shelves. We suggest that using the presented model technique in global ocean models can improve projections of melting and sea level rise.

1 Introduction

Sea level rise is a consequence of human-induced climate change and a threat to coastal communities all around the world (IPCC, 2022). To protect human life and infrastructure in coastal areas, measures must be taken, ideally planned well in advance (IPCC, 2022). This requires reliable projections of sea level rise, which depend on the accuracy of climate models as well as on the understanding of the processes contributing to sea level rise. With a contribution of about 20 %, melting of the Greenland Ice Sheet is one of the main processes (Horwath et al., 2022) and the focus of this paper.

The Greenland Ice Sheet, which has the potential to increase sea levels globally by more than 7 m (Aschwanden et al., 2019), discharges into the ocean at so-called outlet glaciers. Some of these glaciers form ice tongues that float on the water and cover their fjords (Straneo & Cenedese, 2015). Greenland’s largest floating glacier tongue is currently the one of the 79° North Glacier (79NG; Schaffer et al., 2020). It is one of the three main outlets of the Northeast Greenland Ice Stream (Schaffer et al., 2017; Kappelsberger et

al., 2021), holding 1.1 m sea-level equivalent of ice (*i.e.*, its ice could lift global sea levels by 1.1 m if melted entirely, Christmann et al., 2021). Schaffer et al. (2020) estimated that 89 % of the meltwater leaving the 79NG fjord comes from subglacial melting caused by the ocean. Ice melting on land or at the surface only accounts for the remaining 11 % of 79NG meltwater (and even less at other glaciers, see Rignot & Steffen, 2008), which is discharged into the fjord as subglacial runoff at the grounding line. Subglacial melting thins the glacier tongue, which can reduce the buttressing of the ice sheet, *i.e.*, the support of the grounded glacier that is provided by the friction between the ice tongue and the lateral fjord boundaries (Goldberg et al., 2009). With a thinner ice tongue, thus less buttressing, the glacier can flow faster into the ocean, which contributes to sea level rise (Shepherd et al., 2004; Goldberg et al., 2009; Humbert et al., 2022). Furthermore, basal melting can destabilize the ice tongue, which can lead to its breakup (Rignot & Steffen, 2008); in consequence, a lot of ice would be discharged into the ocean (Shepherd et al., 2004). This exemplifies the big role of the ocean in melting the Greenland Ice Sheet (Schaffer et al., 2017) and shows that it is important to understand ice sheet–ocean interactions in glacier fjords like the one at 79° North.

The general idea of ice–ocean interactions under a glacier tongue in Greenland is as follows: Atlantic Intermediate Water (AIW) flows over a sill at the fjord entrance into the glacier cavity as a dense, saline, and warm bottom plume. AIW brings heat into the ice cavity, which is used for melting. The meltwater forms a buoyant plume on the underside of the glacier tongue. This plume causes subglacial melting, transports glacially modified water towards the open ocean, and constitutes the return flow of an overturning circulation within the fjord (Straneo & Cenedese, 2015; Schaffer et al., 2020).

The dense bottom plume and the buoyant subglacial plume are the two main processes in a glacier cavity. However, they are difficult to study, because measurements in Greenland’s fjords are generally sparse (Straneo & Cenedese, 2015), particularly under floating ice tongues, where the ocean is inaccessible to ships and unobservable by satellites. Ice tethered moorings (Lindeman et al., 2020) give some information about processes under the ice, but only at single positions. So numerical models are necessary to gain a detailed understanding of ice sheet–ocean interactions.

A challenge for ocean models is to provide sufficiently high resolution in a glacier fjord to accurately simulate the two plumes. It has been shown that the subglacial plume and particularly its entrainment layer require a vertical resolution of about 1 m or better to correctly model the plume development and the associated melting (Burchard et al., 2022). This is hard to achieve in most ocean models, because of the stark contrast in vertical scales between the fjord depth of several hundred meters and the plume thickness on the order of one to ten meters.

With the vertical coordinates that are commonly used in ocean models, it is unfeasible to achieve a resolution of 1 m along the whole subglacial plume. At 79NG, the plume starts at the grounding line at 600 m depth, so z -coordinate models (Losch, 2008) would require at least 600 vertical layers to resolve the top 600 m of the water column with a 1 m-resolution – much more than can typically be afforded in regional or global models. With σ -coordinates (Timmermann et al., 2012/ed; Gwyther et al., 2020), a high resolution along the whole ice tongue is possible with less layers by activating a zooming towards the ice–ocean interface. However, these terrain-following coordinates have problems when calculating the internal pressure gradient over steep topographic slopes (Haney, 1991; Burchard & Petersen, 1997), which are a typical feature in glacier fjords.

With adaptive vertical coordinates (AVC; Hofmeister et al., 2010), the described problems can be considerably reduced. AVC are terrain-following coordinates that allow with a moderate number of layers a high vertical resolution in places of interest. By minimizing a cost function, AVC adapt automatically to features like stratification, shear, and interfaces (Burchard & Beckers, 2004). This reduces numerical mixing (Klingbeil

et al., 2014; Gräwe et al., 2015) and puts more layers in places where more details need to be resolved, while permitting less vertical resolution in more uniform areas. These coordinates have been used successfully for simulating dense and buoyant plumes in various conditions (e.g., Umlauf et al., 2010; Chegini et al., 2020), but not yet for glacier fjord modeling. We will show that the stratification-zooming feature of AVC is very useful for modeling the ocean circulation under ice shelves, because this provides a high vertical resolution of 1 m in the subglacial plume and the bottom plume with feasible computational cost.

We created an idealized 2D-vertical simulation of the 79NG fjord using AVC together with a melt parametrization (Burchard et al., 2022) that is suitable for high vertical resolution at the ice-ocean interface. To our knowledge, this is the first model to use stratification-zooming coordinates like AVC in a glacier cavity. In addition to testing the performance of AVC under an ice tongue, we use our model to study the sensitivity of the 79NG system to environmental influences. The 20 scenarios of our sensitivity study analyze the effect of the salinity and temperature stratification of the ambient ocean, test the importance of the subglacial discharge, examine the role of the sill, and investigate the influence of roughness or smoothness of the ice tongue.

This paper is organized as follows. The following Section 2 describes our model setup, compares it to the real 79NG fjord, explains our modeling choices including AVC, and describes our analysis methods. Section 3 shows the results of our default simulation (Section 3.1), the performance of AVC (Section 3.2), and the results of our sensitivity study (Section 3.3). This is followed in Section 4 by a discussion of the physical processes we observe in all our numerical experiments and what we learn from these findings about ice-ocean interactions in glacier cavities. We also discuss the role of AVC in obtaining the presented results. Some conclusions and an outlook are given in Section 5. Appendix A lists the mathematical expressions used to build our idealized setup, so that our model can serve as a reference test case for future model developments.

2 Methods

2.1 Idealized 2D model of the 79°N Glacier fjord

We built an idealized numerical ocean model of the 79° North Glacier (79NG) fjord located in Northeast Greenland, using GETM, the General Estuarine Transport Model (Burchard & Bolding, 2002). This model is suitable for our purpose, because

1. GETM comes with adaptive vertical coordinates (AVC) that allow high vertical resolution in areas of interest for low computational cost (Section 2.3);
2. GETM includes state-of-the-art vertical turbulence closure with GOTM (Burchard et al., 1999; Umlauf & Burchard, 2005; Li et al., 2021);
3. GETM has been developed specifically for the coastal ocean and estuaries (Klingbeil et al., 2018).

A glacier fjord is a special type of estuary, in which the subglacial discharge plays the role of a river in a classical estuary (Straneo & Cenedese, 2015; Muilwijk et al., 2022). However, the main source of freshwater is not the subglacial discharge, but the subglacial melting of the floating ice tongue (Schaffer et al., 2020). Since this is the first time that GETM is used for simulating a glacier fjord, we extended the model to include ice tongues and basal melting. The details of this new GETM feature are explained in Section 2.2.

Our GETM setup is a two-dimensional (x, z) representation of the 79NG fjord, of which we consider the main glacier terminus, without the adjacent Dijnphna Sund (Fig. 1a). The ice tongue of 79NG is about 75 km long and 20 km wide; our model has the same width ($L_y = 20$ km) and twice the length ($L_x = 150$ km), to have a sufficiently large

“buffer” between the glacier cavity – which is our main interest – and the open ocean boundary. We resolve the domain with 300 water columns in x -direction ($\Delta x = 500$ m) and one grid point in y -direction; the resolution in z -direction with 100 adaptive layers is explained in Section 2.3. At this horizontal resolution, neither nonhydrostatic effects associated with the plumes nor nonhydrostatic internal waves are resolved, so it is appropriate to use GETM in hydrostatic mode (Klingbeil & Burchard, 2013).

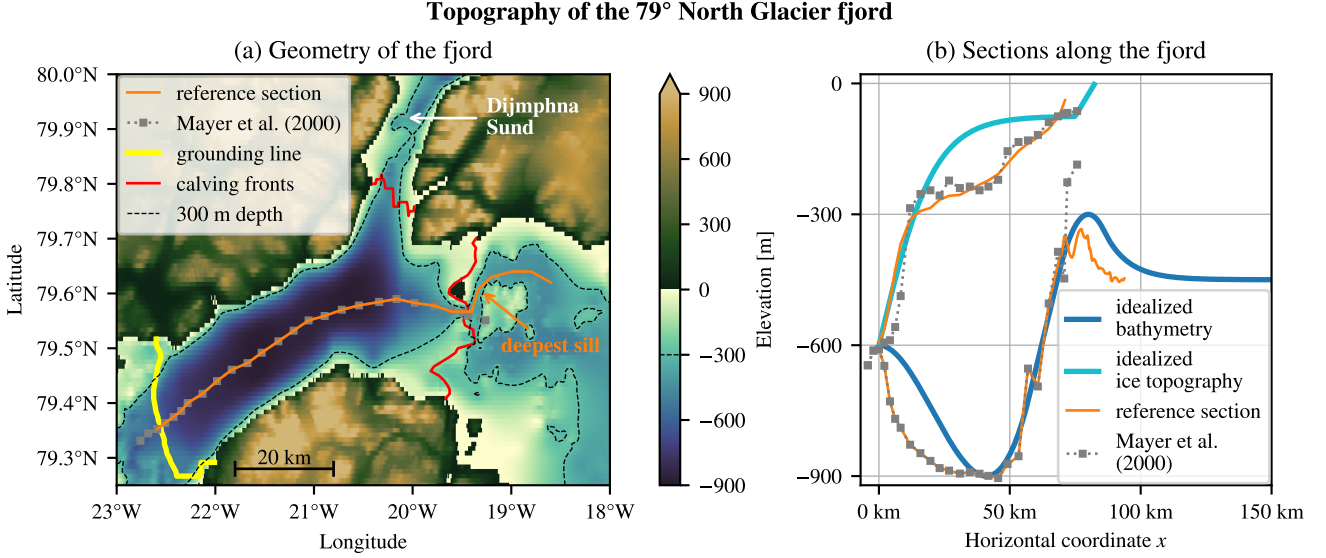


Figure 1. (a) Map of the 79NG fjord and its surroundings showing the bottom elevation from the RTopo-2.0.4 dataset (Schaffer et al., 2019, resolution $30'' = 1/120^\circ$) together with the positions of seismic depth soundings by Mayer et al. (2000). The floating ice-tongue extends from the grounding line in the Southwest to the northern calving front in the Dilmphna Sund and to the main calving front in the East. Atlantic water must pass over a 325 m-deep sill (labeled deepest sill) to flow from the open ocean into the cavity. The reference section is a path from the grounding line towards the open ocean that follows the depth soundings up to the calving front and passes over the deepest sill. (b) Bathymetries and ice topographies along the reference section (from RTopo), along the section by Mayer et al. (2000), and in our idealized 2D fjord model. Note that the deepest sill is the shallowest point along the reference section. The sill depth in our default setup (b) is 300 m, shown as a thin dashed contour in (a).

To construct the bottom topography of our idealized 79NG model, we look at two datasets (Fig. 1). The seismic depth soundings by Mayer et al. (2000) are the most accurate measurements of the bathymetry in the part of the fjord that is covered by the ice tongue. The retreat of the ice tongue in recent decades facilitated more detailed bathymetry measurements near the fjord entrance. In their bathymetric survey, Schaffer et al. (2020) showed that the fjord is separated from the open ocean by a sill that is 325 m deep on its deepest point. Since this sill depth is not representative for the whole width of the fjord (Fig. 1a), we use a shallower sill in our idealized 2D model (Fig. 1b). It is at 300 m depth in our default setup; in our sensitivity study, we analyze the effect of the sill by varying its depth from 200 m to 450 m (Section 3.3.4).

The bathymetry of our idealized model is a smooth concatenation of simple, analytical functions (Fig. 1b): A third-order polynomial connects the grounding line (600 m depth) with the deepest point in the trough (900 m) and continues until it reaches a slope

of 2.5 %. It is then connected linearly to the parabola forming the sill with its maximum (300 m) at 80 km from the grounding line. The parabolic sill goes over into an exponentially decreasing shelf that converges towards a depth of 450 m far offshore. The mathematical details are given in Appendix A1. In our sensitivity experiment without a sill, the linear slope is directly connected with the exponential shelf. Apart from the sill, our model bathymetry only differs markedly from the measured section between the grounding line and the trough (Fig. 1b). Despite this difference, we think that a simpler bathymetry with fewer parameters is preferable to a perfect fit to a single transect for an idealized model such as ours. Also, this deep part of the fjord is mostly inactive in our simulations.

At the grounding line, which forms the left/western boundary of our model ($x = 0$), subglacial discharge enters the glacier fjord. This runoff is implemented in our GETM setup like river input. It is added as freshwater at the local freezing point (-0.45°C , which is less than 0°C due to pressure) to the first water column. We take a constant discharge rate of $70\text{ m}^3\text{ s}^{-1}$ (equivalent to 0.07 mSv reported by Schaffer et al., 2020) in our default setup and varied this value in our sensitivity study (Section 3.3.3). The discharge is distributed uniformly over the whole water column, which is about 6.3 m thick at the first grid center.

At the open boundary on the right/eastern end of our model domain ($x = L_x = 150\text{ km}$), we prescribe the surface elevation η and the ambient ocean stratification. For the former, we use a constant zero elevation. We also tested forcing the model with an M2 tidal oscillation of 0.5 m-amplitude, as measured by Christmann et al. (2021), but our experiments showed that the melt rate is relatively unaffected by the tidal forcing. Therefore, the tide is neglected in the present study. Regarding the open boundary stratification, we use idealized and constant-in-time profiles of temperature and salinity. They are specified by T - and S -values at sea level, at 100 m depth, and at 300 m depth (shown in Fig. 2 and listed in Appendix A3), using linear interpolation in between and constant extrapolation below. In our default setup, the resulting profiles are close to CTD measurements by Schaffer et al. (2020), see the comparison in Fig. 2. We also perform a sensitivity study with modified stratifications (Sections 3.3.1 and 3.3.2).

The model is initialized at rest with a homogeneous stratification equal to the stratification at the open boundary. We run the model with a timestep for the barotropic mode of $\Delta t = 5\text{ s}$, in accordance with the CFL stability criterion, demanding $\Delta t \leq \Delta x / \sqrt{gH_{\max}} \approx 5.3\text{ s}$ (using $H_{\max} = 900\text{ m}$ as the maximum depth of the fjord, see Fig. 1, ignoring the ice cover). We use a split factor of $M = 3$, so that the baroclinic mode is computed every $\Delta t_{3D} = M\Delta t = 15\text{ s}$. While our default setup can be run with a larger baroclinic timestep, the high-melt scenarios give smoother results with a higher temporal resolution, so we decided to use this split factor for all our runs. We activated divergence damping with a diffusion of $A_n = 50\text{ m}^2\text{ s}^{-1}$ on barotropic transports for a conservative smoothing of the sea surface (Vallis, 1992). After a few simulation months, our model approaches a quasi-steady state, in which melting and circulation are almost time-independent. The results shown in this paper are 24 h-averages taken at the end of a six-month simulation and represent the steady state.

2.2 Implementation of glacier ice in GETM

For this study, we added a new feature to GETM that allows simulations of glacier fjords covered by an ice tongue. Where the ice tongue is present, it adds additional pressure (Section 2.2.1), friction (Section 2.2.2), and melt fluxes (Section 2.2.3) to the sea surface. Our implementation allows the ice to move freely vertically, for example with long waves, but it is fixed horizontally. Calving is not included in our model.

In this paper, we use the term *sea surface* to refer to the (moving) upper boundary of the ocean, denoted $\eta = \eta(x, t)$ and measured from $z = 0$ with positive values upwards. Depending on the x -position, the sea surface can be the ice-ocean interface or

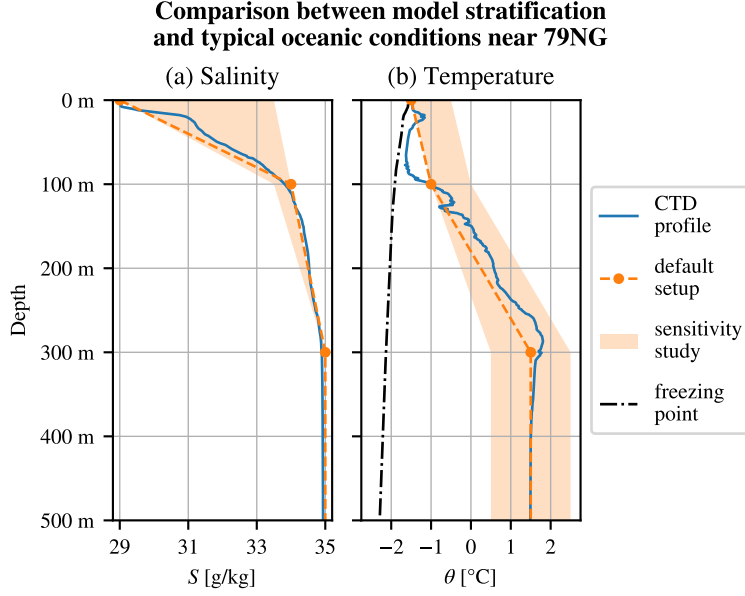


Figure 2. Stratification used in our model as boundary and initial conditions compared with salinity (a) and temperature (b) measurements near the 79NG fjord. The shaded area marks the minimum and maximum values tested in our sensitivity study. The CTD profile was taken in 2017 on RV *Polarstern* (Kanzow et al., 2018) and represents a typical ambient ocean stratification for 79NG (Schaffer et al., 2020, see their Fig. 1a for the location of the profile). The freezing point of saline water in (b) corresponds to the shown CTD profile. We used the Python package gsw (TEOS-10; IOC et al., 2010) to convert pressure to depth and to compute the freezing temperature.

the atmosphere–ocean interface. Furthermore, we use the term *sea level* to refer to the level $z = 0$, which is the initial position of the atmosphere–ocean interface.

2.2.1 Pressure due to ice and initial sea surface elevation

Under glacier ice, the pressure at the ice–ocean interface is the atmospheric pressure (constant in our model) plus the contribution from the weight of the ice tongue (Losch, 2008). We can represent this pressure due to floating ice as $p_i = g\rho_i h_i$, where h_i is the thickness of the ice column and ρ_i its (homogeneous) density (Table 1). Both $h_i(x)$ and ρ_i are constant-in-time in our implementation and serve as input parameters to the model.

To initialize our model in an equilibrium state, we must prescribe the initial surface elevation $\eta_0 = \eta(t = 0)$ such that the ocean with the floating glacier ice is in hydrostatic balance. This is the case if the water displaced by the ice tongue has the same weight as the ice tongue (Archimedes’ principle). For an initially homogeneous stratification with (water) density $\rho(z)$, this condition can be expressed as:

$$\rho_i h_i = \int_{\eta_0}^0 \rho(z) dz. \quad (1)$$

In our setup, we prescribe the lower ice edge η_0 (see below) and determine h_i such that (1) is fulfilled, which has the consequence that we have slightly different ice thicknesses h_i for different stratifications $\rho(z)$ (difference to the default setup is always less than 20 cm). Note that a corollary of (1) is the handy rule-of-thumb $\eta_0 \approx -0.9h_i$, which says that 90 % of an ice column is below sea level and 10 % is above.

Table 1. Settings and parameters of our model in the default scenario

Name of the parameter	Symbol	Value
Geometry:		
length of the fjord	L_x	150 km
width of the fjord	L_y	20 km
roughness length of the sea floor	z_0	1.5×10^{-3} m
roughness length of the ice tongue	$z_{0,\text{ice}}$	1×10^{-2} m
Glacier:		
ice temperature	T_i	-20°C
ice density	ρ_i	920 kg m^{-3}
subglacial discharge		$70 \text{ m}^3 \text{ s}^{-1}$
Numerics:		
vertical model layers		100
horizontal resolution	Δx	500 m
barotropic timestep	Δt	5 s
baroclinic timestep	Δt_{3D}	15 s
divergence damping	A_n	$50 \text{ m}^2 \text{ s}^{-1}$
Thermodynamics:		
heat capacity of sea water	c	$3985 \text{ J kg}^{-1} \text{ K}^{-1}$
heat capacity of glacial ice	c_i	$1995 \text{ J kg}^{-1} \text{ K}^{-1}$
latent heat of fusion	L_i	$3.33 \times 10^5 \text{ J kg}^{-1}$

Given the initially horizontally homogeneous (and stable) ocean stratification, we initialize the ice in its equilibrium position by evaluation of the integral in (1). As the simulation runs, the stratification changes due to basal melting, subglacial discharge, ambient water inflow, and mixing, so the equilibrium position of the ice changes as well. Since the ice in our model can move freely vertically with the convergence and divergence of transports, it will adapt to the changing stratification. The setups presented here reach a quasi-steady state, in which the glacier tongue has found a new equilibrium position, which is slightly (on the order of millimeters) different from the initial position.

In our idealized 79NG fjord model, we prescribe a smooth ice–ocean interface between the grounding line at 600 m depth and the calving front at $x = 75$ km, where the ice–ocean interface is 75 m below sea level. For the idealized ice shape, we choose a hyperbolic tangent with a maximum slope of 2.5 % at the grounding line (see Appendix A2 for the mathematical details). This fits well with the measured ice slope near the grounding line (see the reference section in Fig. 1b). Since subglacial melting is strongest in this area (Schaffer et al., 2020), we believe it is important to reproduce the ice topography well near the grounding line and accept that the idealized shape differs from observations at mid-depths, as we prefer a simple, analytical ice shape over a perfect fit to a single transect.

At the calving front, a big slope is to be avoided, as it would cause problems with the terrain-following coordinates, because the water near the calving front is strongly stratified, so individual grid cells would span a large density range. Therefore, we extend the ice–ocean interface with a linear 1 %-slope until sea level is reached. We also tested higher slopes at the calving front, but the model results were poorer, because the horizontal flow below the calving front was too much diluted by passing through too many cells. Thus, we use a slope instead of a vertical wall at the calving front. This is a deviation from the real system, but an acceptable one, since our focus lies on processes inside the glacier cavity, which are not much affected by this difference.

2.2.2 Surface friction

Where the ocean is covered by glacier ice, there is a no-slip boundary condition at the sea surface (Burchard et al., 2022). This friction at the ice–ocean interface is implemented in GETM according to the law-of-the-wall with a roughness length $z_{0,\text{ice}}$, similar to bottom friction. In our default scenario, we use the value $z_{0,\text{ice}} = 0.01$ m. The effects of smoother or rougher ice are tested in our sensitivity analysis (Section 3.3.5).

2.2.3 Parametrization of subglacial melting

We implemented the subglacial melt formulation by Burchard et al. (2022). This parametrization, based on the three-equation model (D. M. Holland & Jenkins, 1999), is suitable for high vertical resolutions under the ice. In our free-surface model, meltwater is added like precipitation as a real freshwater flux (Huang, 1993) to the uppermost grid cell of the water column with a melt rate v_b (in m s^{-1}). There is no salt flux, $f_b^S = 0$, because the melted glacier ice is assumed to have zero salinity. There is, however, a temperature flux at the ice–ocean interface:

$$f_b^T = v_b \left[\frac{c_i}{c} (\theta_b - T_i) + \frac{L_i}{c} - \theta_b \right]. \quad (2)$$

In the squared bracket, the first term corresponds to the energy necessary for heating up the glacial ice from its core temperature T_i to the melt layer temperature θ_b ; the second term is the latent heat of the phase change from ice to water; the last term appears because water is exchanged between ice and ocean, *i.e.*, the ice–ocean interface is a non-material interface in our model (Jenkins et al., 2001). The values of the constants in (2) are given in Table 1. The melt layer is a thin layer at the ice–ocean interface, that is not resolved but parametrized in our model. For a detailed discussion, see Burchard et al. (2022).

The here-described implementation of melting differs from that used by Burchard et al. (2022), because their 1D model has a rigid lid. In a rigid lid model, the water volume cannot increase, so a virtual salt flux through the ice–ocean interface is needed to get the diluting effect of basal melting on salinity, and a virtual temperature flux is needed instead of (2). However, the more realistic approach is adding meltwater explicitly (Huang, 1993; Jenkins et al., 2001), without a salt flux and with only a real temperature flux, as we do it in this study. Even though melting increases the water volume in our model, the ice volume does not decrease. To allow for a decreasing ice volume and a thinning ice tongue, ice dynamics would have to be modeled as well. Instead, we assume that there is a balance between basal melting of the ice tongue and the discharge of glacier ice from land into the ocean.

2.3 Adaptive vertical coordinates

Our GETM setup uses adaptive vertical coordinates (AVC) described by Burchard and Beckers (2004) and Hofmeister et al. (2010). These coordinates are well-suited for representing surface-attached buoyant plumes (Chegini et al., 2020) and dense bottom currents (Hofmeister et al., 2010; Umlauf et al., 2010). AVC are topography-following coordinates, in which the vertical distribution of the model layers changes with time. The temporal change of model layers is implemented by minimizing a cost function depending on the model state, particularly the stratification. The coordinates adapt in a way that there are more layers in regions with higher stratification. This ensures high vertical resolution in areas of strong vertical density gradients and minimizes numerical mixing (Hofmeister et al., 2010; Klingbeil et al., 2014; Gräwe et al., 2015).

In the 79NG fjord, important density differences exist in two locations: (i) Between the meltwater plume at the ice–ocean interface and the ambient water below, and (ii) between the bottom current and the cavity water above (Schaffer et al., 2020). With AVC

we can obtain high resolutions in both of these plumes and particularly in their entrainment layers, without a large increase in computational cost ($< 10\%$ more computation time compared to σ -coordinates). For this, we configured AVC so that they zoom towards stratification and towards the sea surface. An explicit bottom-zooming is not required, because the stratification-zooming itself provides sufficiently high resolution in the bottom plume (Section 3.2). Activating the zooming towards the seafloor would also result in high resolution in the deep trough of the glacier fjord and on the continental shelf outside the ice cavity, even though these parts are mostly inactive in our simulations. Thus, we do not activate it and opt instead for an even higher resolutions near the ice–ocean interface, which is important for the accurate representation of melting (Burchard et al., 2022). While 50 coordinate levels would be sufficient to achieve a vertical resolution better than 2 m in the plume under the ice, we present in this paper simulations with 100 AVC layers to show the plumes and the circulation in great detail.

2.4 Analysis of plume-averaged quantities

To analyze the entrainment of the subglacial plume, we compute its bulk properties, *i.e.*, the vertically averaged plume characteristic. We want to diagnose the bulk values following the ideas by Arneborg et al. (2007) in the modified form for plumes under ice shelves (Burchard et al., 2022):

$$\bar{b}D = \int_{-\infty}^{\eta} b(z) dz, \quad (3)$$

$$\bar{b}D^2 = 2 \int_{-\infty}^{\eta} b(z) z' dz, \quad (4)$$

$$\bar{u}D = \int_{-\infty}^{\eta} u(z) dz, \quad (5)$$

where $z' = \eta - z$ is the distance from the ice–ocean interface, $b(z) = -g[\rho(z) - \rho_0]/\rho_0$ is the buoyancy, and ρ_0 is the ambient ocean density. However, the above equations have been derived in a 1D setting with the assumptions that the ambient water below the plume is homogeneous (with density ρ_0) and stagnant ($u = 0$), which is not the case in our 2D model. So an integration to $-\infty$ or to the sea floor at $z = -H$ would not make sense, because it would include several different water masses in the plume analysis. Instead, we choose an integration depth $h_0 > 0$, consider the water mass at $z = \eta - h_0$ as the ambient water, and use the following modified formulas

$$\bar{b}D = \int_{\eta-h_0}^{\eta} b(z) dz, \quad (6)$$

$$\bar{b}D^2 = 2 \int_{\eta-h_0}^{\eta} b(z) z' dz, \quad (7)$$

$$\bar{u}\bar{b}D = \int_{\eta-h_0}^{\eta} u(z)b(z) dz, \quad (8)$$

as definitions of plume thickness D , plume buoyancy \bar{b} , and plume velocity \bar{u} . Note that dividing (7) by (6) gives D , dividing (8) by (6) gives \bar{u} , and dividing (6) by D gives \bar{b} . We take as ρ_0 the density linearly interpolated from cell centers to $z = \eta - h_0$; a vertical interpolation gives considerably smoother graphs for the bulk values than taking the density of the grid cell containing $z = \eta - h_0$. The factors of $b(z)$ and \bar{b} in (8) ensure that the integral gives more weight inside the plume than outside, where $b(z)$ is smaller since the local density $\rho(z)$ is closer to that of the ambient water, ρ_0 . We use velocities horizontally interpolated to cell centers (instead of cell interfaces) in (8), so that all bulk values are defined on cell centers.

The bulk values of velocity \bar{u} , buoyancy \bar{b} , and thickness D allow to compute the Froude number

$$\text{Fr} = \frac{|\bar{u}|}{\sqrt{|\bar{b}|D}}, \quad (9)$$

which is a non-dimensional number relating the velocity of the plume to the phase speed of long waves at the plume interface (Arneborg et al., 2007; Burchard et al., 2022). The Froude number tells us whether the flow is supercritical ($\text{Fr} > 1$) or subcritical ($\text{Fr} < 1$).

Following P. R. Holland and Feltham (2006), the bulk values can be used to formulate a conservation equation for the plume volume:

$$\partial_t D + \partial_x(D\bar{u}) + \partial_y(D\bar{v}) = v_b + v_e, \quad (10)$$

where the terms on the right-hand side are the melt rate v_b and the entrainment velocity v_e . For our 2D system ($\partial_y = 0$) in steady state ($\partial_t = 0$), (10) implies

$$\bar{u}\partial_x D = -D\partial_x \bar{u} + v_b + v_e, \quad (11)$$

which means that the plume thickness increases in x -direction by flow convergence ($-D\partial_x \bar{u}$), melting, and entrainment. Since the melting is computed by our numerical model, we can reformulate (11) to diagnose the entrainment (Burchard et al., 2022):

$$v_e = D\partial_x \bar{u} + \bar{u}\partial_x D - v_b. \quad (12)$$

The choice of the integration depth h_0 requires some considerations. It must be chosen such that (as long as the plume is attached to the ice) $z = \eta - h_0$ lies always outside the plume in a weakly stratified region, but not too far away, so that $\rho_0 = \rho(z = \eta - h_0)$ is actually the density of the water surrounding the plume. To find a suitable integration depth, a visual inspection of the model result is helpful. The identified value is a good choice if the computed bulk values are stable, *i.e.*, they do not vary much for small variations of h_0 . In our default scenario, this is the case for $h_0 = 10$ m. However, the precise choice of h_0 is not critical for the results.

For the analysis of the dense bottom plume, we use an analogous approach, but with integration from the sea floor at $z = -H$ to $z = -H + h_0$, and with $z' = H + z$ being the distance from the sea floor in (7). We take $h_0 = 20$ m as the integration height for the bottom plume, since its typical thickness is around two-times that of the subglacial plume.

2.5 Analysis of the overturning circulation

A key property of a glacier fjord is the strength of its overturning circulation, often reported in milli-Sverdrup ($1 \text{ mSv} = 1000 \text{ m}^3 \text{ s}^{-1}$). We take as a measure of the overturning strength the maximum (in absolute value) of the (volume) stream function over the sill ($x = 80$ km). The stream function ψ is defined by

$$\partial_z \psi = uL_y, \quad (13)$$

$$\partial_x \psi = -wL_y, \quad (14)$$

and the condition that $\psi = 0$ on the sea floor; L_y is the (constant) width of the fjord (Table 1). Numerically, we diagnose ψ by summing the horizontal transports $u\Delta zL_y$ (defined on cell edges) from the sea floor to the sea surface, which follows from (13) and naturally satisfies $\psi = 0$ at the bottom. Then (14) is automatically fulfilled thanks to the 2D continuity equation, $\partial_x u + \partial_z w = 0$. Since the model results shown in this paper are in steady state, the contour lines of the stream function ψ are trajectories.

3 Results

In this section, we present at first the steady state of our default scenario (Sections 3.1 and 3.2), then we perform a sensitivity study with varying physical parameters (Section 3.3).

3.1 Circulation and melting in the default scenario

In our default model setup, which is an idealized representation of the present day situation at 79NG as observed by Schaffer et al. (2020), we find an estuarine-like circulation in the glacier cavity (Fig. 3a–d). This circulation is made up of two gravity plumes: strong, turbulent, and focused currents that are driven by density differences. One is a buoyant plume at the lower ice edge, driving the melting of the ice tongue and transporting glacially modified water out of the fjord into the ambient ocean (blue in Fig. 3a). The other plume – a dense bottom current – brings warm and salty Atlantic Intermediate Water (AIW) from the open ocean over the sill into the glacier cavity (red in Fig. 3a). The strength of the overturning circulation is 39 mSv (Fig. 3b), consistent with the value of (46 ± 11) mSv obtained from hydrographic measurements (Schaffer et al., 2020).

Subglacial melting creates a layer of cold water just below the ice along the whole glacier tongue (Fig. 3c). This meltwater is transported away from the glacier and introduces a layer of cold water into the ambient ocean at depths of around 90 m to 95 m below sea level. Minimum temperatures offshore the calving front are below -1.5°C at 94 m depth. Apart from this layer and its immediate surroundings, the temperature stratification offshore the sill is mostly in equilibrium with the imposed open ocean conditions. As the flow of AIW from the open ocean into the glacier cavity is hindered by the sill, the cavity water becomes colder than the open ocean water by mixing with meltwater (inset of Fig. 3c).

Salinity differences are the main drivers of the circulation in the 79NG fjord (Fig. 3d). On the one side, the subglacial plume rises along the ice tongue because it is fresher, thus lighter than the water inside the cavity. On the other side, AIW flows down the bottom slope into the glacier cavity because it is saltier, thus denser than the cavity water. Comparing the water at the same depth on both sides of the sill, we see that the cavity water, which is a mixture of AIW with meltwater, is at least 0.1 g kg^{-1} fresher than AIW (inset of Fig. 3d). Offshore the sill, the salinity stratification is almost horizontally homogeneous and in equilibrium with the imposed conditions of the open ocean.

Along the whole ice tongue of 79NG, the basal meltrate is positive, *i.e.*, no freezing appears in our simulation (Fig. 3e). We find the strongest melting of 58 m yr^{-1} close to the grounding line and a mostly monotonic decrease of the meltrate afterwards. The meltrate reaches practically zero ($< 0.1 \text{ m yr}^{-1}$) at around 42 km from the grounding line. The rest of the ice tongue has an average meltrate of less than 0.01 m yr^{-1} . The position where the melting stops coincides with the place where the subglacial plume detaches from the ice tongue (see Section 3.1.1). The meltrate averaged over the whole ice tongue is 12.3 m yr^{-1} (corresponding to $20.3 \text{ km}^3 \text{ yr}^{-1}$) in our model, consistent with the value of $(10.4 \pm 3.1) \text{ m yr}^{-1}$, or $(17.8 \pm 5.2) \text{ km}^3 \text{ yr}^{-1}$, estimated by Schaffer et al. (2020) based on measurements. Accordingly, also the percentage of subglacial discharge in the total meltwater production at 79NG is similar between our model (9.8 %) and observations (11 %; Schaffer et al., 2020). This shows that basal melting is by far the dominant freshwater source in the glacier fjord.

3.1.1 The buoyant subglacial plume

The subglacial plume starts at the grounding line ($x = 0$), where subglacial runoff is discharged into the cavity. Since this discharge is fresher than the water in the fjord, it is positively buoyant and rises along the lower ice edge. We observe in our model that two opposing processes modify the plume water while rising. On its upper side, the plume

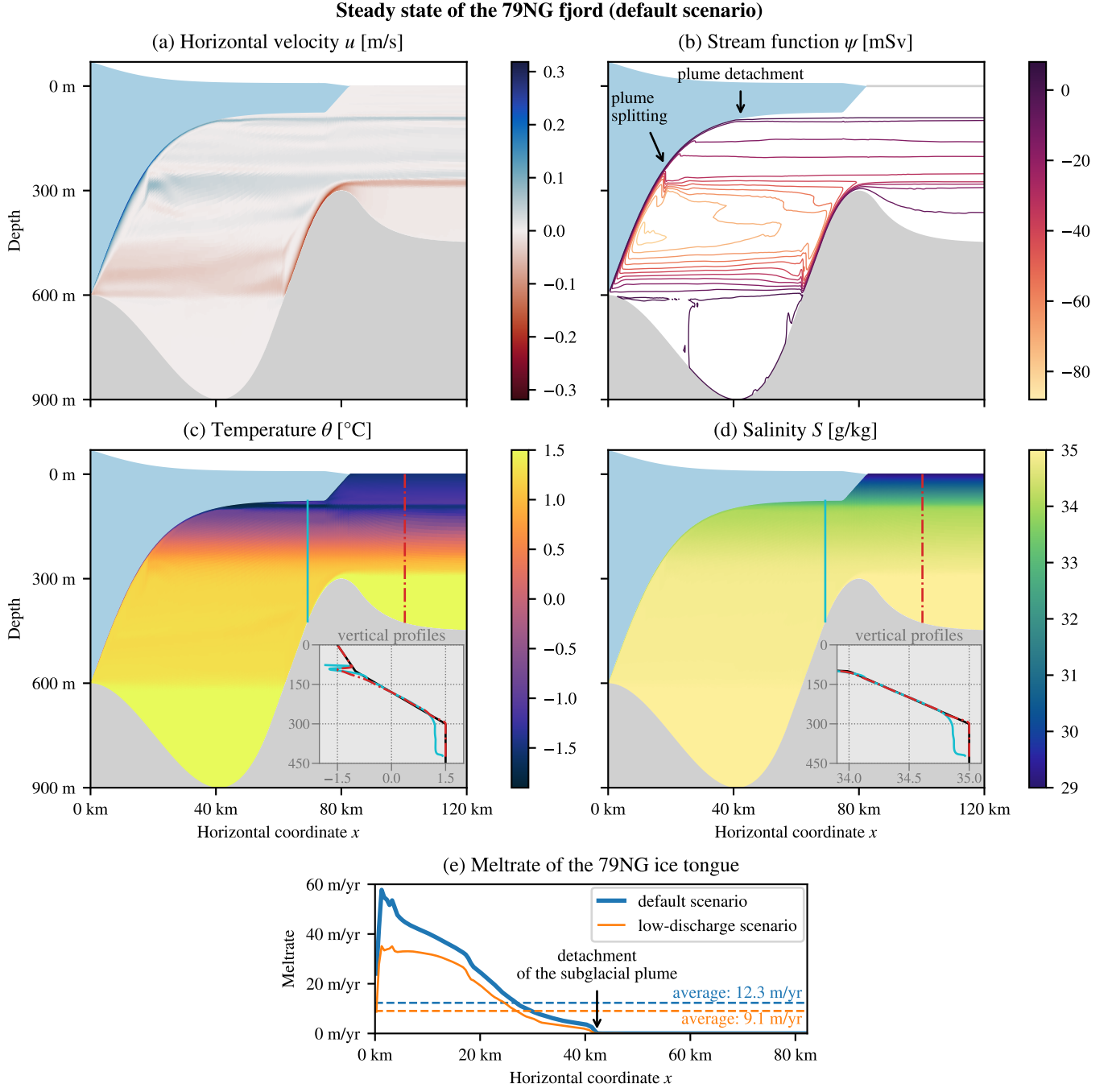


Figure 3. Model results in steady state for our default scenario of the 79NG fjord showing horizontal velocity (a), stream function (b), temperature (c), salinity (d), and meltrate (e). Insets in panels (c) and (d) show vertical profiles of temperature and salinity, respectively, at positions on both sides of the sill marked with vertical lines in the same colors as the graphs; conditions at the open boundary are shown in black for comparison. The thin orange line in panel (e) corresponds to a sensitivity experiment, in which the subglacial discharge is reduced by an order of magnitude compared to the default scenario (Section 3.3.3).

causes melting of the ice tongue due to friction, which adds cold and fresh meltwater to the plume. On its lower side, ambient water is entrained upwards into the plume by turbulent mixing, thus making it saltier and warmer. This way, entrainment transports heat towards the ice and amplifies the melting (Burchard et al., 2022). As the plume rises, it passes through ever lighter surrounding water and reaches a point where its density equals that of the ambient water (Fig. 4a). This is between 95 m and 100 m below sea level. At this level, the subglacial plume detaches from the ice tongue, propagates horizontally away from the glacier, and transports glacially modified water out of the fjord (Fig. 3a–c).

Before this detachment, the plume splits up a number of times. The first splitting occurs at 18 km from the grounding line (Fig. 5). Until there, the plume was rising through well-mixed water, allowing it to grow and thicken rapidly by entrainment. However, around the depth of the sill (300 m), the stratification changes and the ambient water becomes stably stratified (Fig. 5d). The lower part of the plume consisting of denser water overshoots its neutral level, falls about 70 m down, rises slightly again, and finds its neutral level near $z = -290$ m, where it propagates away from the ice (Fig. 5a,b). This creates a buoyancy oscillation visible in the streamlines (Fig. 3b). However, the oscillation is strongly damped, because the plume mixes with ambient water during its ascent and descent (Fig. 5c), thereby reaching neutral buoyancy quickly (Fig. 5d). Similar though smaller splits of the plume can be observed several times until the plume detachment. This creates a vertical velocity profile with a number of velocity peaks between the depth of the calving front and the depth of the sill (Fig. 3a).

Prior to the splitting of the plume, its thickness increases from $D = 3$ m at a distance of 5 km from the grounding line to about $D = 5$ m at $x = 18$ km (Fig. 4a). Over this distance, the plume becomes more buoyant and increases its vertically-averaged velocity \bar{u} to a maximum of 0.22 m s^{-1} (Fig. 4b,c). When the plume splits, its velocity drops and so does its buoyancy \bar{b} , because the ambient water below the plume becomes lighter. After the splitting, the plume thickens more slowly and reaches $D = 6$ m at $x = 40$ km, just before its detachment from the ice. When it detaches, the plume buoyancy drops again (Fig. 4c), meaning that the plume density is similar to the ambient density, which is the reason for the plume detachment. Note that the buoyancy does not go to zero because the formulas to compute \bar{b} (Section 2.4) are only applicable while the plume is within 10 m from the ice edge; afterwards the thin lines in Fig. 4b–d represent the properties of the water just below the ice.

Entrainment at the plume base is only positive until the plume splits for the first time (Fig. 6a). The plume thickening afterwards is mainly due to flow convergence (Fig. 6a) in consequence of the plume slowing down (Fig. 4b). It is not due to entrainment, because after the initial phase, the entrainment velocity v_e is negative and detrainment appears (Fig. 6a). So instead of taking up ambient water, the plume in total loses water to the stratified interior of the cavity (Fig. 3). Correspondingly, the vertical velocity under the plume is negative, *i.e.*, downward (Fig. 6c). The detrained water forms an out-flowing layer below the plume (Fig. 6b).

Our interpretation of the detrainment is that initially, the weakly stratified water in the deep part of the cavity allows strong turbulence to develop (Fig. 6d), leading to high entrainment rates of $E = v_e/\bar{u} = \mathcal{O}(2 \times 10^{-4})$ and rapid plume thickening (Fig. 4a), consistent with the initial plume development and entrainment reported by Burchard et al. (2022). When the plume arrives in the more stratified upper part of the cavity, the reduced turbulence is insufficient to sustain the thick plume. Comparing turbulent kinetic energy (TKE) in the entrainment part with the detrainment part, we see that in the latter case, TKE is clearly reduced at the ice–ocean interface, at the plume base, and below the plume (Fig. 6d). So the turbulence might be too weak to further entrain ambient water against gravity, and instead the plume detrains water. This manifests in the first plume splitting near $x = 18$ km and the subsequent smaller splits as described above.

Details of the subglacial plume (a–d) and of the bottom plume (e–h)

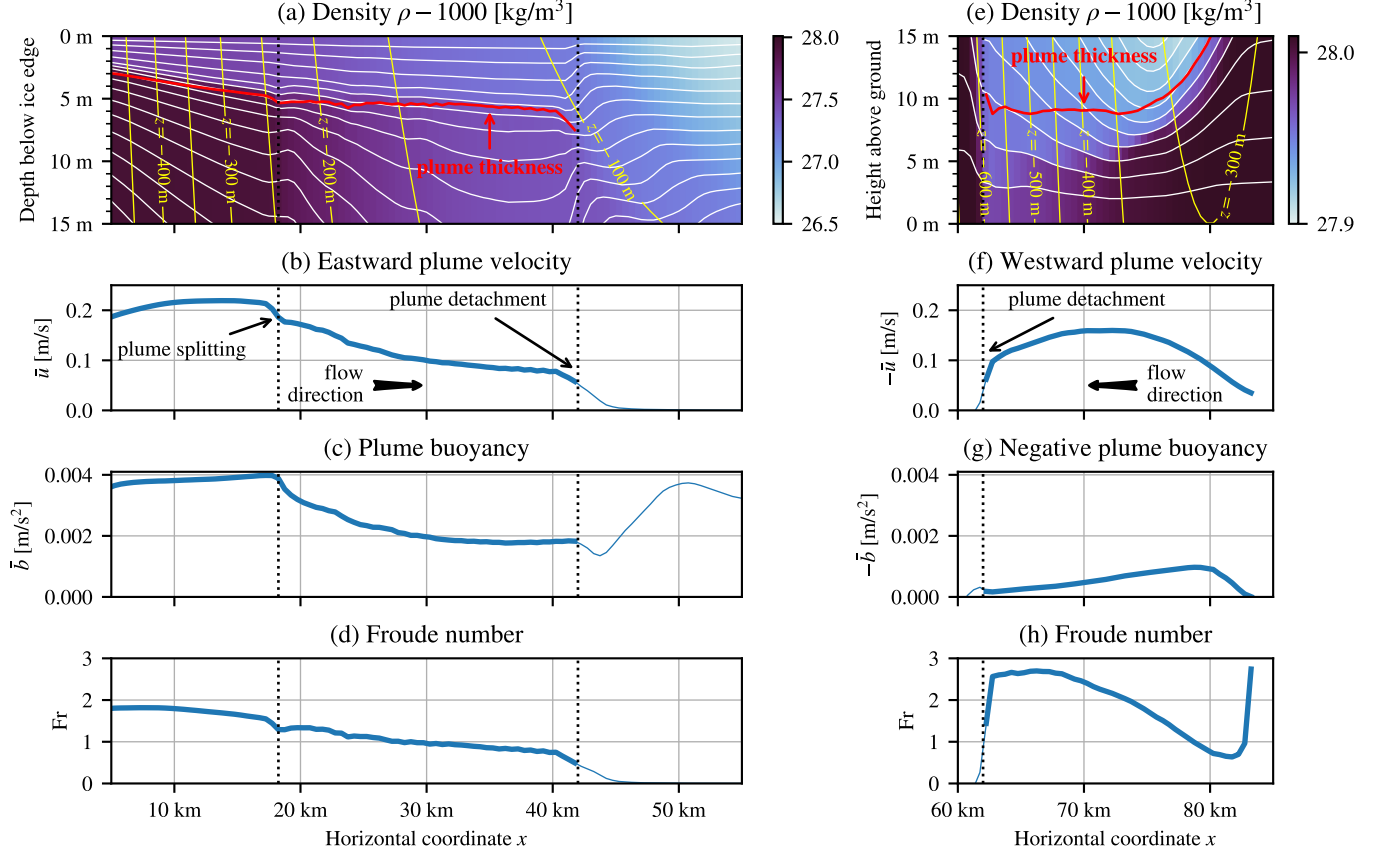


Figure 4. Detailed view of the buoyant plume (a–d) and of the dense plume (e–h) (default scenario). The first row shows density (a) in the 15 m just below the ice–ocean interface and (e) in the 15 m just above the sea floor; note the different starting points of the colorbars. White lines are vertical coordinate levels (cell edges of the model grid) and emphasize the high resolution of about 1 m obtained by AVC in the entrainment layers of both plumes. Depth contours in yellow show that the plume water goes horizontally after the detachment. The red lines represent the thicknesses D of the plumes before their detachments, which are marked by dotted vertical lines. The thicknesses (a,e) and bulk values (b–d,f–h) were calculated as explained in Section 2.4. Note that the bulk values in panels (f) and (g) have opposite signs than those in (b) and (c), because the plumes go in opposite directions and are oppositely buoyant. After the plume detachments, bulk values are shown as thin lines, because they do not represent the plumes anymore; instead, they show the averaged properties of the uppermost 10 m under the ice (b–d) or the lowermost 20 m above the seafloor (f–h).

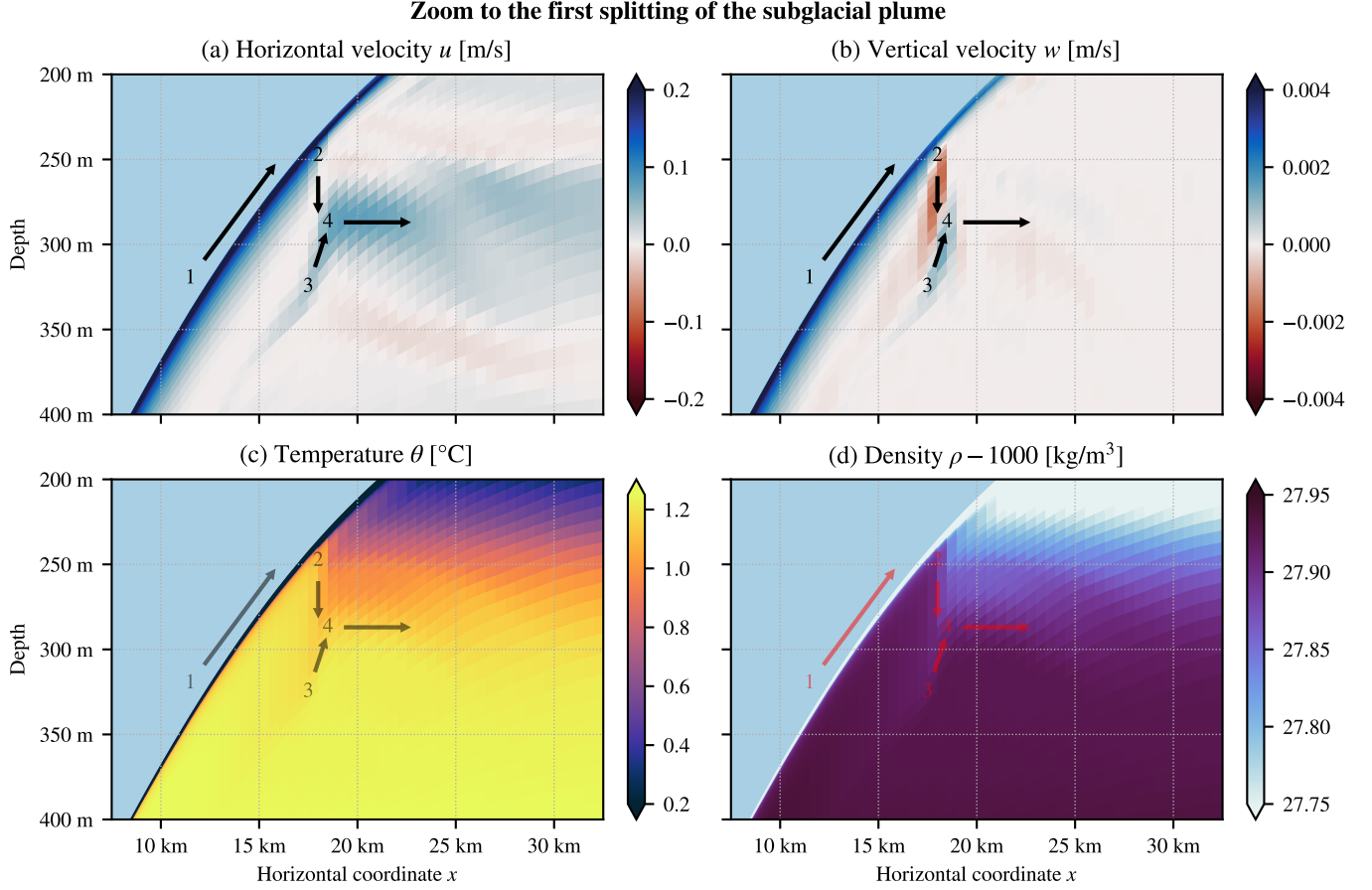


Figure 5. Zoom to the first splitting of the subglacial plume (default scenario). The arrows represent the flow direction resulting from the combined effects of the horizontal (a) and vertical (b) velocity components: (1) The plume rises along the ice tongue; (2) the lower part of the plume falls down from about 250 m depth to about 320 m depth, while becoming slightly colder and lighter due to mixing with ambient water; (3) the plume rises to about 290 m depth and (4) flows horizontally away from the ice tongue.

For most of its path along the ice, the plume is supercritical ($Fr > 1$; Fig. 4d). It transitions to subcritical flow ($Fr < 1$) around 30 km from the grounding line.

3.1.2 The dense bottom plume

The bottom plume in the 79NG fjord consists of AIW coming from the open ocean. With a density of 1028.0 kg m^{-3} (Fig. 4e), this is the densest water mass in our system, as well as the warmest and saltiest (Fig. 3c,d). It flows from the sill at $x = 80 \text{ km}$ down into the cavity, following the bathymetry. As long as the bottom slope increases, the plume accelerates up to a vertically-averaged velocity of $\bar{u} = -0.16 \text{ m s}^{-1}$ (Fig. 4f). Due to this flow divergence, the plume thins from 15 m over the sill to 9 m thickness six kilometer downstream (Fig. 4e).

While flowing down the bottom slope, the plume entrains ambient cavity water, which has a lower density since it contains meltwater (Fig. 4e). In consequence, the plume density and buoyancy (in absolute value) decrease (Fig. 4g). Similar to the subglacial

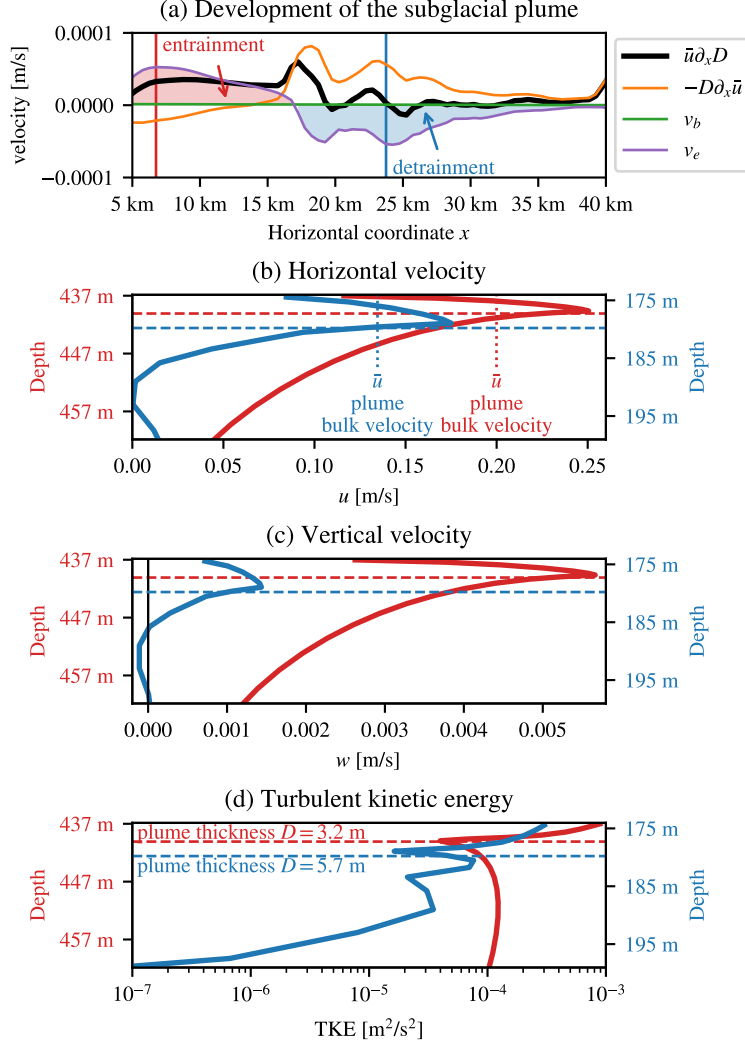


Figure 6. Development of the subglacial plume thickness D before the detachment from the ice tongue, with areas of entrainment and detrainment highlighted (a); vertical profiles at positions near maximum entrainment (red) and detrainment (blue), showing velocity components (b,c) and turbulent kinetic energy (d) in the 25 m under the ice (default scenario). The colored graphs in (a) represent the processes acting on the plume thickness: flow convergence (orange), subglacial meltwater (green, close to zero), and entrainment velocity at the plume base (purple); summed together, they give the thicker black line, see (11). For the calculation of the graphs in (a), plume thickness D and bulk velocity \bar{u} were smoothed with a running average of window size ± 1 km.

plume, the bottom plume transports water below its neutral depth. The water then rises again and adjusts in an oscillating way to its level of neutral buoyancy (Fig. 3b), before propagating horizontally away from the bathymetry. This way, the bottom plume fills the cavity with (partially mixed) AIW over a depth range of 450 m to 600 m (Fig. 3a). At about 600 m below sea level, the plume has detached completely from the bottom. It cannot propagate further down, because the entrainment of cavity water made the plume lighter than the water in the trough below 600 m depth. The water in the deep trough is dense because it consists of almost pure AIW with only little meltwater. This is because (i) meltwater enters the cavity only at depths where the ice tongue is present, and (ii) the meltwater is not mixed far below the grounding line (600 m) due to the absence of strong motion there.

The bottom plume is mostly supercritical ($Fr > 1$; Fig. 4h). Only for a short distance around the peak of the sill, where the bottom plume is slow and thick, the Froude number is less than one.

Outside the cavity, just offshore the sill, even some AIW below the sill level moves upward and flows over the sill (Fig. 3b). This overflow is driven by an internal pressure gradient that is vertically homogeneous, since the water on the upstream side of the sill is unstratified. The phenomenon of upward acceleration of dense water against gravity is called aspiration and commonly observed in fjords (Inall & Gillibrand, 2010).

3.2 Performance of the adaptive vertical coordinates (AVC)

AVC is one feature of our model that has not been employed before in simulations of glacier fjords. Our setup uses 100 vertical layers that adapt automatically to the stratification, as explained in Section 2.3. This way, we reach high vertical resolutions in both plumes.

The vertical resolution in the subglacial plume is everywhere close to 1 m and even better in the entrainment layer at the plume base (white lines in Fig. 4a). Thus, AVC achieve the necessary resolution to represent the entrainment of the ambient water into the plume correctly (Burchard et al., 2022). Since the model layers adapt to and follow the plume, its water is advected mostly along the layers and not across. The plume is always resolved by five layers or more while it is attached to the ice, which allows to preserve the plume properties well. When the plume detaches from the ice, AVC still manage to follow the flow of the meltwater to some extent by partially bending in the horizontal direction (Fig. 4a).

The calving front presents a challenge for AVC. As terrain-following coordinates, they must connect the lower ice edge to the sea level, a difference of 75 m in depth. However, the flow under the calving front is horizontal and the density is horizontally homogeneous, so there is necessarily a divergence between coordinates and plume. By stretching the calving front over 7.5 km as explained in Section 2.2.1, the vertical position of the ice–ocean interface changes gradually enough, so that the coordinates manage to adapt to the plume to some extent and preserve its properties well (see the inset of Fig. 3c). However, a slight dilution of the plume as it passes under the calving front and through several layers can still be seen (Fig. 3a–c).

Similar to the subglacial plume, also the incoming plume of Atlantic Water is resolved by several layers with a thickness on the order of 1 m (Fig. 4e). As the plume propagates down the slope, it thins due to velocity divergence, so the number of layers in the plume reduces.

The high resolution in the vicinity of the ice and the bottom comes at the expense of thicker layers in the interior of the glacier cavity. While the vertical layers are less than 10 m thick in most areas, there are up to 15 m-thick layers in the middle of the water col-

umn in places where the fjord is deepest. However, we believe that this is a good trade-off, because (i) the thick layers appear in areas where the velocities are small and the water column is only weakly stratified, and (ii) we obtain very thin layers in the dynamically relevant parts.

3.3 Sensitivity studies

We now explore how the results change compared to the default scenario for modified environmental influences. Key properties of all presented scenarios are summarized in Table 2.

Table 2. Summary of the presented simulations

Scenario	Meltrate (m yr^{-1})	Overturning (mSv)	Runoff
default	12.3	39.2	9.8 %
high salinity	12.6	40.1	9.6 %
low salinity	10.2	32.2	11.6 %
AIW: -1.0 K	7.6	35.1	15.0 %
AIW: -0.5 K	10.0	39.0	11.8 %
AIW: $+0.5$ K	15.5	43.8	8.0 %
AIW: $+1.0$ K	19.0	47.7	6.6 %
PW: $+0.5$ K	12.3	39.3	9.9 %
PW: $+1.0$ K	12.2	38.9	9.9 %
AIW & PW: $+0.5$ K	15.3	42.0	8.0 %
AIW & PW: $+1.0$ K	18.7	47.1	6.7 %
discharge 1/10-th	9.1	25.7	1.5 %
discharge doubled	14.3	49.9	15.8 %
sill at 200 m	9.2	21.7	12.7 %
sill at 250 m	11.1	31.2	10.7 %
sill at 350 m	13.2	57.1	9.2 %
sill at 400 m	13.3	78.1	9.1 %
no sill	13.4	107.2	9.1 %
smooth ice (z0m)	16.1	52.5	7.7 %
rough ice (z0p)	5.6	30.8	19.4 %
Observation	10.4 ± 3.1	46 ± 11	11 %

Meltrate is the subglacial meltrate averaged over the whole ice tongue. Overturning is the strength of the circulation measured above the sill. Runoff is the percentage of subglacial discharge in the total meltwater outflow (discharge plus melting) of the fjord. Observation cites the values reported by Schaffer et al. (2020). AIW stands for (the temperature of) Atlantic Intermediate Water, PW for Polar Water.

3.3.1 Influence of the ambient ocean salinity

The subglacial plume detaches from the ice tongue and transports meltwater out of the fjord towards the open ocean at a depth of around 95 m below sea level in our default scenario. This sensitivity study shows that the depth depends strongly on the salinity stratification of the ambient ocean, which is imposed at the open boundary of the model. When the salinity of the upper water column is increased, the plume propagates further along the ice tongue and detaches higher up. With lower salinities above the sill, the plume does not propagate as far up and detaches earlier.

This relation is exemplified by the two sensitivity experiments shown in Fig. 7 in comparison with the default case. For the high salinity scenario, we increased the surface salinity from 29 g kg^{-1} to 33.5 g kg^{-1} , so that we obtain a linear salinity stratification in the upper 300 m of the water column (Fig. 7b). With this stratification, the plume detaches at around 50 m below sea level (Fig. 7a). In the low salinity case, we kept the surface value at 29 g kg^{-1} but decreased the salinity at 100 m depth from 34 g kg^{-1} to 33.5 g kg^{-1} (Fig. 7f). Then most of the plume detaches between 125 m and 150 m of depth (Fig. 7e). These experiments also show that the plume detachment is not caused by the abruptly changing stratification that is in the default scenario at a similar depth as the detachment (Fig. 7c,d).

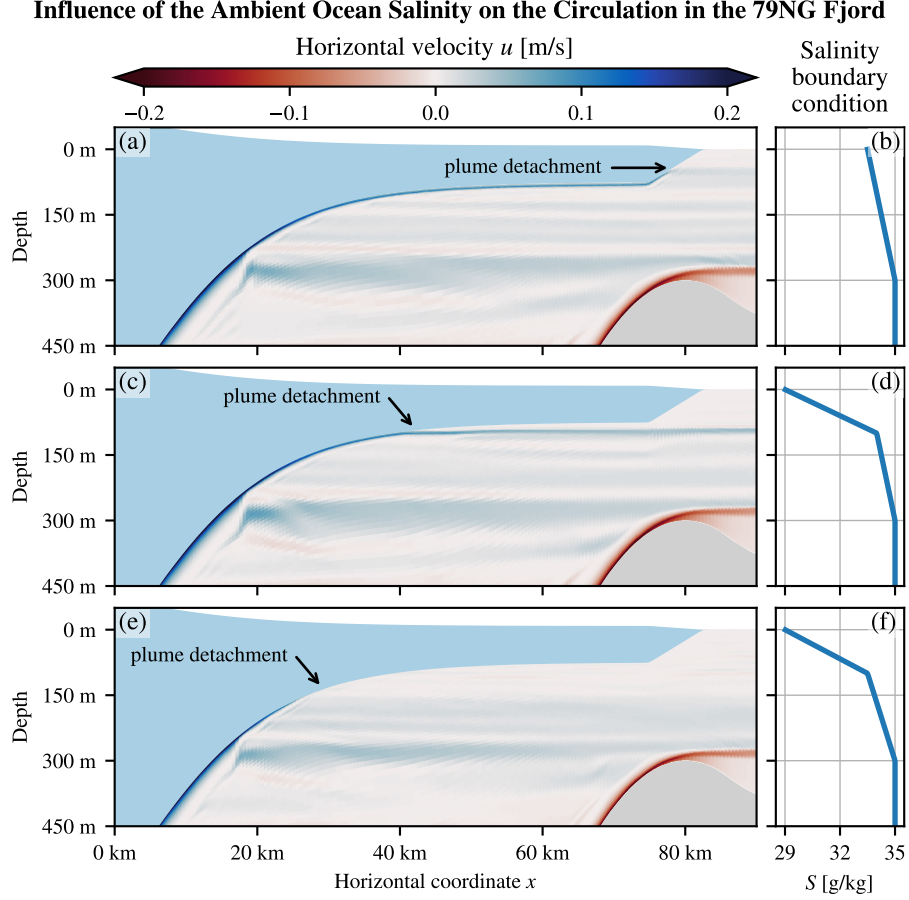


Figure 7. Experiments on the sensitivity of 79NG to the open ocean stratification, with higher salinity (a,b) than in our default scenario (c,d) as well as lower salinity (e,f). For higher salinities above the sill, the subglacial plume propagates further along the ice tongue and detaches higher up. The salinity at the level of plume detachment is always around 33.7 g kg^{-1} . When the plume detaches early (e), a weaker secondary plume develops above.

In fact, it is the salinity of the open ocean that determines the depth where the plume detaches. The salinity at the detachment level is $(33.7 \pm 0.1) \text{ g kg}^{-1}$ in all three scenarios. We also tested a stratification with a minimum salinity of 34 g kg^{-1} (not shown), in which case the plume never detaches from the ice tongue but reaches sea level. The reason that the detachment depth depends strongly on salinity is that at this level, the

plume density equals that of the ambient ocean, which is set primarily by salinity in the 79NG fjord.

For the deeper half of the ice tongue, the plume developments and meltrates are basically identical between our sensitivity experiments, but they differ in the upper 300 m. At the plume detachments, the subglacial meltrates drop to almost zero, which shows again that the subglacial plume is responsible for the bulk of basal melting. In the scenario with the plume detachment at great depths, a small second plume develops above the main detachment, causing some more melting with meltrates up to 0.7 m yr^{-1} before detaching near 100 m depth (Fig. 7e). Only in the scenario with a late plume detachment, we observe meltrates above 0.2 m yr^{-1} along the whole ice tongue up to the calving front. However, note that the plume development as it propagates up the calving front in this scenario (Fig. 7a) is not entirely realistic, because the calving front is sloping in our model and not vertical (Section 2.2.1).

3.3.2 Influence of the ambient ocean temperature

We investigate the influence of the imposed temperature stratification at the open ocean boundary by varying the temperatures of Polar Water (PW) and Atlantic Intermediate Water (AIW) individually as well as together. In our model, PW occupies the upper 100 m of the water column and has in the default scenario a linear temperature profile with -1.5°C at sea level and -1.0°C at 100 m depth (Fig. 2b). AIW fills the water column below 300 m depth and has a vertically homogeneous temperature of 1.5°C by default. In between 100 m and 300 m, we apply a linear temperature gradient. In our sensitivity study, we increase the temperatures of AIW and/or PW by 0.5 K or 1.0 K. We also decrease AIW temperatures by 0.5 K and 1.0 K. Note that we cannot make PW colder, because the surface temperature is just above freezing in our default scenario (Fig. 2b).

We observe that the AIW temperature has a clearly larger impact on the glacier cavity than variations of PW temperature. With increasing AIW temperature, the subglacial meltrate increases along the whole ice tongue (Table 2) and the point at which the plume detaches moves upward. For AIW temperatures of 0.5°C , the plume detaches below 130 m, for 2.5°C above 90 m depth. This can be explained by the increased temperature forcing, which causes more melting and thereby a lighter plume that rises faster and further. Interestingly, in the deep part of the cavity, the thickness of the subglacial plume is not much altered by temperature differences, although this is the part where AIW is present.

The effects associated with increased PW temperatures are much smaller. Cavity circulation and both plumes look practically the same as in the default scenario. The only (small) difference we observe is in the detachment point of the subglacial plume. It moves about 2 m down for a PW temperature increase of 0.5 K and about 3 m (compared to default) for a 1.0 K-increase. This makes sense because the upper part of the water column is lighter for warmer PW, so the plume reaches its neutral buoyancy earlier. Since subglacial melting almost stops when the plume detaches, the overall meltrate is slightly lower for higher PW temperatures (Table 2). However, note that our model does not simulate calving, which can be intensified in warmer water.

When we increase the temperatures of both AIW and PW together, thus making the whole water column warmer, we observe a combination of the effects described above. The results look similar to those with only increased AIW temperatures, but the subglacial plume detaches at a slightly deeper level.

3.3.3 Role of the subglacial discharge

The meltwater discharged at the grounding line has an important influence on subglacial melt. In our default scenario, we prescribe a constant subglacial discharge of $70 \text{ m}^3 \text{ s}^{-1}$,

which is the value reported by a field campaign (Schaffer et al., 2020), and we find a clear, peaked meltrate maximum just after the grounding line. In contrast, if we reduce the discharged water volume in our model by an order of magnitude to $7 \text{ m}^3 \text{ s}^{-1}$, we observe a flatter melt distribution after the grounding line with a lower and rather constant meltrate over the first 10 km (Fig. 3e). Interestingly, after the splitting of the subglacial plume, the melt distributions look similar for low discharge and normal discharge (Fig. 3e). Also, the position of the plume detachment from the ice tongue is not much different. These observations suggest that the subglacial discharge has mostly an impact on the early development of the plume, while further away from the grounding line, the plume development is mostly determined by subglacial melting and the ambient ocean stratification.

Due to the decreased subglacial melting in scenarios with lower subglacial discharge, the cavity water is warmer, saltier, and denser. This has the effect that the dense bottom plume does not propagate as far down the slope and detaches earlier from the bottom. Also, both plumes are thinner and slower than in the default scenario. The strength of the overturning circulation is reduced by about one third to 26 mSv for a discharge of $7 \text{ m}^3 \text{ s}^{-1}$ (Table 2).

We observe the opposite effects when we increase the subglacial discharge: The meltrate increases; the cavity water becomes colder, fresher, and lighter; the plumes are thicker and faster. Doubling the discharge to $140 \text{ m}^3 \text{ s}^{-1}$ increases the overturning strength by about one fourth (relative to default scenario) to 50 mSv and the average meltrate by about one sixth to 14.3 m yr^{-1} (Table 2).

In our model, we cannot reasonably increase the subglacial discharge arbitrarily. For example, with a discharge of $700 \text{ m}^3 \text{ s}^{-1}$ (ten-times the default), the large amount of meltwater leaving the cavity cannot be transported across the open boundary, because the prescribed conditions at the open boundary correspond to the default scenario, which has lower discharge and melting. This causes a density front near the open boundary, which is physically unstable and prevents the system from reaching a steady state. Nevertheless, the model stays numerically stable, even in such a non-equilibrium situation.

3.3.4 Role of the sill

Our model allows us to test a hypothesis made by Schaffer et al. (2020) based on their hydrographic measurements. They claim that the bathymetry of the 79NG fjord constrains the heat transport from the open Atlantic ocean into the glacier cavity. According to Schaffer et al. (2020), the height of the sill at the fjord entrance determines how much warm AIW flows into the fjord, and in turn how much heat is available for subglacial melting. In our idealized 2D model, we can easily modify the sill height (default: 300 m below sea level) or remove the sill completely and check which impact it has.

We find that the cavity water is clearly colder with a higher sill than with a lower sill or without a sill (Fig. 8a,b, see also Fig. 3c). The higher the sill, the stronger the temperature contrast between the water in the cavity and the water on the continental shelf. Consequently, the meltrate is larger if the sill is at greater depths and *vice versa* (Fig. 8c,d). Interestingly, the meltrate is not larger over the full length of the ice tongue, but mostly in the $(20 \pm 5) \text{ km}$ after the grounding line, where the ice is at great depths. The melting of the thinner part of the ice tongue is not much influenced by the sill, neither is the position of the plume detachment from the ice. When the sill is at 350 m below sea level or deeper, the meltrate is almost independent of the sill depth (Fig. 8c,d). At this depth, the sill cannot effectively prevent the warm AIW from entering the cavity anymore.

So our simulations show that indeed the sill height constrains the heat transport into the cavity and thereby determines the meltrate of the 79NG ice tongue. This “sill effect” almost ends at a depth of about 350 m, measured from sea level.

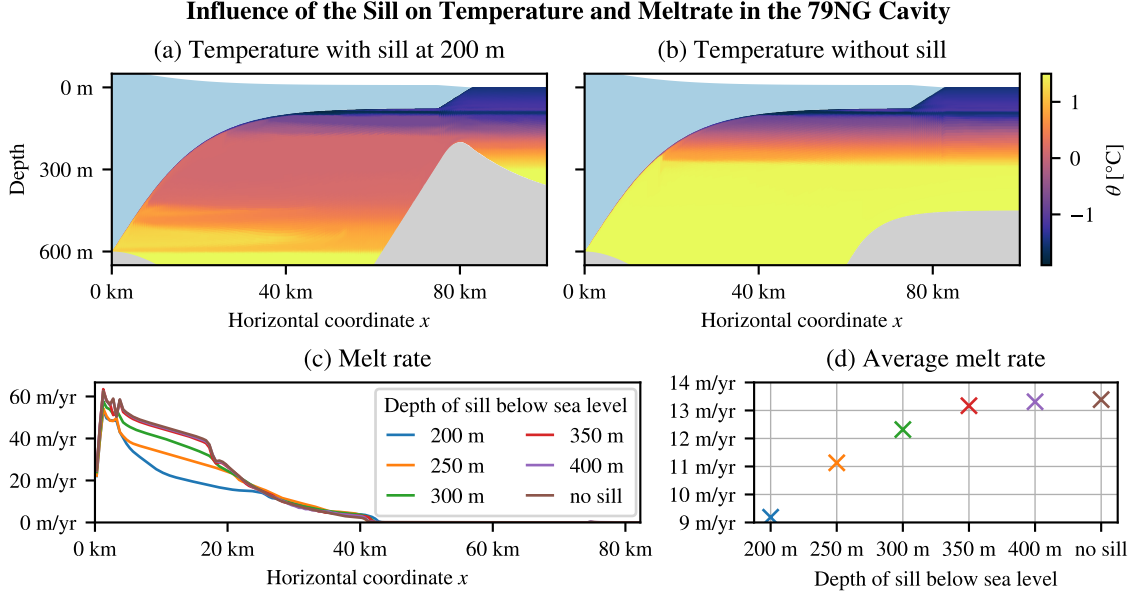


Figure 8. Temperature in the glacier cavity in a modified 79NG fjord with a high sill (a) and with no sill (b), as well as subglacial melt rate of the 79NG ice tongue with x -resolution (c) and in spatial average (d) for different sill depths (including no sill). When the sill is higher, *i.e.*, with a lower sill depth, less warm water can flow into the cavity, so the melt rate is lower. Note that the continental shelf offshore the cavity is at 450 m below sea level, so a sill depth of 450 m means no sill.

3.3.5 Roughness length

In our setup, the smoothness or roughness of the ice tongue on its underside is modeled by a roughness length, $z_{0,\text{ice}}$. This parameter has the value 0.01 m in our default scenario, but it is poorly known which value is realistic for a given ice shelf (P. R. Holland & Feltham, 2006). To test the sensitivity of the 79NG system on this value, we increased the roughness length by a factor of ten ($z_{0,\text{ice}} = 0.1$ m, scenario z0p) and decreased it by a factor of ten ($z_{0,\text{ice}} = 0.001$ m, scenario z0m). We also tested intermediate values to ensure that our observations are actually tendencies as reported below.

Our model results show that the shorter the roughness length, the larger the melt rate and the stronger the overturning circulation (Table 2). Due to the higher melting, the subglacial plume becomes colder (Fig. 9c,d), fresher, and more buoyant. It accelerates faster and has a higher velocity under the ice and after its detachment (Fig. 9a,b). Also the dense bottom plume is faster with a shorter roughness length (not shown). Even though the subglacial plume is fresher, the parameterized melt layer at the ice–ocean interface (Section 2.2.3) is actually saltier for smoother ice.

In the scenario z0p, most of the plume detaches from the ice tongue already at a depth of 200 m and leaves the fjord at this level, while the outflow at 100 m-depth is much weaker (Fig. 9b,d). Initially, the plume thickens quickly but detrains strongly around 23 km from the grounding line, so after this point, the plume is thinner than in the other two scenarios. In the scenario z0m, the plume is everywhere thinner than in the default scenario. One reason is that the entrainment is reduced because it must overcome a stronger stratification between plume and cavity water. So the high buoyancy of the plume reduces the entrainment of ambient water and thereby reduces the plume thickening, as

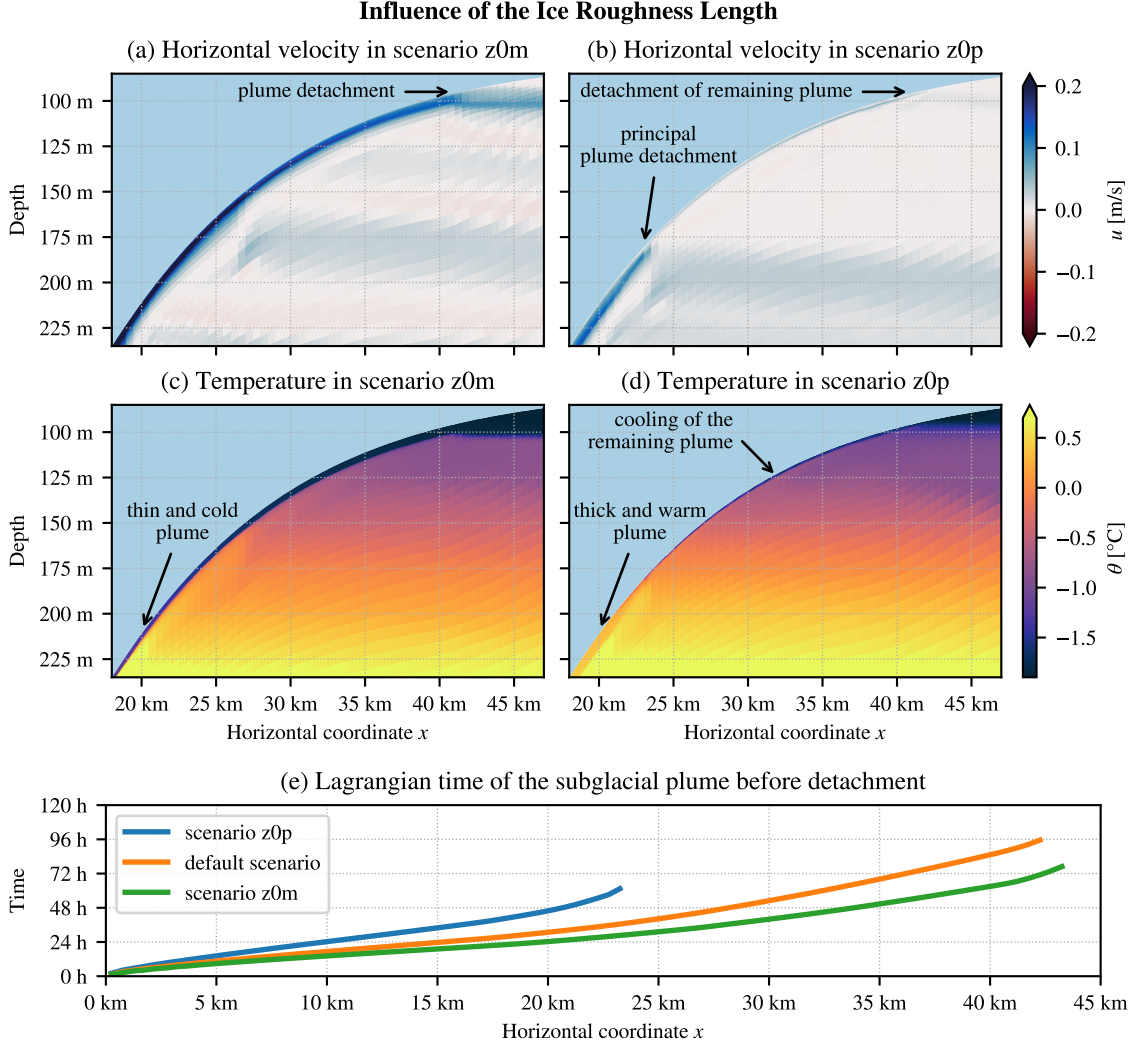


Figure 9. Influence of the roughness length of the ice tongue, $z_{0,ice}$, on the circulation (a,b) and the temperature (c,d) below the ice tongue as well as on the Lagrangian time of the subglacial plume (e). The Lagrangian time t , defined as the integral of $dt = dx/\bar{u}$, is shown up to the (principal) plume detachment, see panels (a), (b), and Fig. 3; this position is identified by a clear reduction of under-ice velocity u and plume velocity \bar{u} .

730 predicted by classical two-layer entrainment theory. Another reason is that the stronger
731 acceleration of the plume leads to a divergence, which also thins the plume.

732 Our findings are consistent with the study of a subglacial plume by Burchard et
733 al. (2022), who analyzed the same scenarios in a 1D model. They also observed thicker
734 plumes for longer roughness lengths and less entrainment for shorter roughness lengths.
735 Regarding subglacial melting, Burchard et al. (2022) observed at the beginning of the
736 plume development higher melt rates in the scenarios with smoother ice. After about one
737 week, the relation is reversed and the melt rate increases with the ice roughness, as pre-
738 dicted by equilibrium theory. However, our 2D model suggests that the subglacial plume
739 in the 79NG fjord does not actually reach this equilibrium state. The plumes in all an-
740 alyzed scenarios need – in a Lagrangian sense – less than four days to reach the point
741 at which they detach from the ice tongue (Fig. 9e). Thus, our results correspond to the

initial plume development in the study of Burchard et al. (2022), where meltrates are higher for smoother ice.

4 Discussion

In large-scale ocean models without explicitly resolved glacier cavities, meltwater from fjords is often introduced at the sea surface (e.g., Stolzenberger et al., 2022). Our model results show that this is generally not realistic. In fact, the bulk of meltwater leaves the 79NG fjord in our default scenario between 90 m and 100 m below sea level (Section 3.1 and Fig. 3a–c). This level depends primarily on the stratification of the ambient ocean, which is mainly set by salinity. Even a relatively small change in the upper ocean salinity can alter the outflow depth of glacially modified water by 50 m (Section 3.3.1 and Fig. 7). The temperature stratification also influences the outflow depth, but less dramatically, as our sensitivity study shows (Section 3.3.2). On the other hand, the outflow depth is almost unaffected by the subglacial discharge and by the sill at the fjord entrance, despite their big influence on subglacial melting and overturning circulation in the cavity (Sections 3.3.3 and 3.3.4). If the base of the ice tongue had a higher roughness, the outflow around 95 m depth would be weaker but still at the same depth as for smooth ice (Section 3.3.5 and Fig. 9a,b). We suspect that the outflow depth of meltwater does not change much with seasons, because the fjord properties that have a strong seasonality are the subglacial runoff (Lindeman et al., 2020; Schaffer et al., 2020) and the ocean surface temperature, which both have little impact on the outflow level. Whether the subsurface stratification at 79NG, which is important for the outflow depth, shows seasonal variability, is still unknown, but the existing mooring data shows no clear signature of a seasonal cycle (Lindeman et al., 2020; Schaffer et al., 2020, and own analysis of their datasets). Longer time series of measurements at 79NG are necessary to answer this question.

The depth at which meltwater leaves the glacier fjord is not only relevant for the export of glacially modified water but also for the development of the ice tongue. Our simulations show that most subglacial melting occurs while the subglacial plume is at the ice–ocean interface. When the plume detaches, the meltrate drops to almost zero. This happens roughly at the same level as the meltwater outflow. Thus, oceanographic measurements of the depth of glacially modified water near a glacier fjord can be used to infer which part of the glacier tongue is likely to show high basal meltrates. This information can be helpful for a decision of where to install measurement stations on a floating ice tongue to monitor ice thickness changes.

At the depth where the subglacial plume propagates away from the ice tongue, the vertical coordinate levels in our model accumulate. This ensures that the water properties of the plume are preserved over long distances with little spurious mixing. It is achieved automatically by the stratification zooming of AVC. No *a priori* knowledge of the position of plume detachment is needed, which is an important difference to non-adaptive coordinates that can achieve high vertical resolutions in pre-defined regions. Moreover, AVC change the vertical layer distribution with time, for example in simulations with tides or other time-varying forcings that alter the stratification.

With z -coordinates, which are often used to model the ocean under an ice tongue or an ice shelf (e.g., Losch, 2008), it would be difficult to obtain equally detailed simulations of the cavity circulation and in particular of the subglacial plume. Due to their step-wise manner of resolving the ice–ocean interface, z -coordinates are usually too diffusive to preserve the plume over longer distances. Without a well-preserved plume, an analysis of the entrainment rate as shown in Fig. 6 would not be feasible. An insufficient representation of the plume development has also implications on the accuracy of the computation of basal meltrates (Burchard et al., 2022). Furthermore, a good simulation

of meltwater export from the fjord into the open ocean demands a good preservation of the plume properties with minimal spurious mixing. This can be provided by AVC.

While AVC (Hofmeister et al., 2010) have a number of characteristics, the main feature used in our setup is their capability to zoom towards stratification. This enables high resolutions in the entrainment layers of both plumes and allows the coordinates to follow the outflow to a reasonable extent, so that glacially modified water can be transported far offshore. This stratification zooming could be combined with other modeling approaches like vertical Lagrangian remapping or the Arbitrary Lagrangian-Eulerian (ALE) method. In these methods, Lagrangian motion of the model grid is followed by a regrid step, in which the coordinate surfaces are moved back to prescribed target positions; the physical fields are then mapped onto this new grid in a remap step (Griffies et al., 2020). The target coordinate layout could be prescribed based on the ocean stratification in the current model state. Such an approach would combine the advantages of ALE with the advantages of stratification zooming shown in this paper.

As for terrain-following coordinates in general, the calving front presents a challenge for AVC. Our setup uses a gentle slope instead of an almost vertical wall at the ice front to make sure that the plume is well preserved as it leaves the cavity. This part of the ice tongue could possibly be simulated more realistically by a modification of the cost function that determines the zooming of AVC. Instead of zooming to stratification and the sea surface, it might be advantageous to zoom only to stratification and the ice-ocean interface but not to the atmosphere-ocean interface. This way, more layers could be available at the calving front to allow a high calving front slope as well as a good preservation of plume properties. Since AVC (Hofmeister et al., 2010) have not been developed with glacier tongues in mind, and this paper presents their first application to an ice cavity, such a possibility has not yet been implemented. It should however be kept in mind that processes at the calving front are strongly non-hydrostatic in nature and therefore cannot be sufficiently reproduced with classical ocean models anyway.

While our idealized 79NG fjord model shows qualitatively realistic dynamics and processes under the glacier tongue, its quantitative results should be taken with a grain of salt, as exemplified by our sensitivity study on the sill depth (Section 3.3.4). We observe that the meltrate of the ice tongue (Fig. 8) and the strength of the overturning circulation in the cavity (Table 2) are very sensitive to the depth of the sill at the fjord entrance, which is 300 m in our default setup. However, no single value can be entirely realistic, because in the real system, the sill is not at the same depth over the whole fjord width (Fig. 1a). The depth of the sill, which is the shallowest point that inflowing water must cross, depends on the path from the open ocean into the cavity. It can be as deep as 325 m below sea level but also shallower (see Fig. 1 and Schaffer et al., 2020). Since this cross-fjord variability cannot be reproduced in 2D, the quantitative results of a 2D model can only be approximations.

5 Conclusions and Outlook

We developed a numerical ocean model of a glacier fjord in 2D with high horizontal and vertical resolution. The fjord and its forcing were built to resemble 79NG in an idealized, analytical way (Fig. 1 and 2). Quantitative results of our default simulation are a good approximation of reality. In particular, the subglacial meltrate and the strength of the overturning circulation are consistent between our model and measurements at the glacier (Table 2). Thanks to the simplicity of the model, its qualitative results (Fig. 3), which we explored further in a sensitivity study, will also hold for other glacier cavities.

Our model shows that the buoyant plume, which develops on the underside of the ice tongue, is responsible for the bulk of subglacial melting. When the plume reaches neutral buoyancy and detaches from the ice, basal melting almost stops. At this level, which

is about 95 m below sea level in our present-day (default) scenario, the plume transports meltwater out of the fjord towards the open ocean. The detachment depth is set primarily by the stratification of the ambient ocean, particularly its salinity (Fig. 7).

Furthermore, we confirmed that the depth of the sill at the fjord entrance has a big influence on the melt rate and the overturning strength in the fjord. With a deeper sill, the dense bottom plume brings more warm Atlantic water into the cavity and thus more heat is transported towards the ice tongue (Schaffer et al., 2020), which intensifies subglacial melting. In case of 79NG, this sill effect ends at around 350 m depth (Fig. 8).

The two plumes that make up the estuarine circulation in the glacier cavity are resolved by our model in great detail (Fig. 4 and 6), thanks to the stratification-zooming of AVC (Hofmeister et al., 2010). We showed for the first time that with this modeling approach, a vertical resolution of less than 1 m in the entrainment layer of the buoyant plume under an ice tongue can be achieved (Fig. 4), which is important for the correct representation of subglacial melting and plume development (Burchard et al., 2022). The computational cost compared to non-adaptive σ -coordinates is increased by less than 10 % (Section 2.3), which is much cheaper than increasing the number of vertical layers. Further advantages of AVC are that they minimize the pressure gradient error (Hofmeister et al., 2010; Gräwe et al., 2015) and that they follow the plumes to some extent, which preserves the properties of the outflowing water mass well (Fig. 3). We believe that the application of AVC in more ocean models will mean an improvement to the way processes under ice tongues and ice shelves are simulated. When stratification zooming is used together with a melt parametrization that is suitable for high vertical resolutions (Burchard et al., 2022), this can refine projections of ice sheet melting and glacier stability.

Given the successful demonstration of AVC in an idealized 2D glacier cavity, a next step should be to extend this setup into a realistic 3D model of the 79NG fjord. This should include resolving the across-fjord dimension with the same high resolution as the along-fjord direction, using the real geometry and topography of the fjord, as well as forcing the regional ocean model with actual observational or reanalysis data. Such a setup will allow to study effects that have been neglected so far, *e.g.*, the Coriolis effect, and will back up our qualitative results with accurate quantitative assessments.

Appendix A Analytical description of the setup

Our setup is built to resemble the 79NG fjord in an idealized way that can be completely described by simple, analytical functions. Here we give the mathematical expressions of these functions for the future use of our setup as a reference test case.

A1 Model bathymetry

The definition of the default model bathymetry is based on the following points:

- (P1) grounding line ($x = 0$) at $z_{\text{gline}} = -600$ m,
- (P2) deepest point in the trough at $(x_{\text{trough}}, z_{\text{trough}}) = (41 \text{ km}, -900 \text{ m})$,
- (P3) highest point of the sill at $(x_{\text{sill}}, z_{\text{sill}}) = (80 \text{ km}, -300 \text{ m})$,
- (P4) continental shelf far offshore ($x \rightarrow \infty$) at $z_{\text{shelf}} = -450$ m,

together with the following conditions on the bottom slope dz/dx :

- (S1) The slope is zero at the grounding line: $dz/dx = 0$ for $x = 0$.
- (S2) The slope is at most 2.5 % in absolute value: $|dz/dx| \leq s_{\text{max}} = 0.025$ for all $x \in [0 \text{ km}, 150 \text{ km}]$.
- (S3) The slope is a continuous function.

The last condition ensures that the bathymetry $z(x)$ is smooth, the other six conditions are derived from bathymetric measurements (Mayer et al., 2000; Schaffer et al., 2020), see Fig. 1. The combination of these seven conditions fully defines the glacier cavity as the concatenation of a third-order polynomial for the grounding line and the trough, a second-order polynomial for the sill, and a first-order polynomial in between, as explained in the following. With a choice of the transition point from sill to continental shelf (given below), also the exponentially decreasing shelf is fixed.

Conditions (P1,P2,S1) imply that the third-order polynomial going from the grounding line through the trough is

$$z(x) = a_{\text{trough}}x^3 + b_{\text{trough}}x^2 + z_{\text{gline}}, \text{ with} \quad (\text{A1})$$

$$b_{\text{trough}} = 3 \frac{z_{\text{trough}} - z_{\text{gline}}}{(x_{\text{trough}})^2}, \text{ and} \quad (\text{A2})$$

$$a_{\text{trough}} = -\frac{2}{3} \frac{b_{\text{trough}}}{x_{\text{trough}}}. \quad (\text{A3})$$

In consequence of (S2), the trough ends at x_0 such that

$$\frac{dz}{dx}(x_0) = 3a_{\text{trough}}x_0^2 + 2b_{\text{trough}}x_0 = s_{\text{max}}, \text{ where} \quad (\text{A4})$$

$$z_0 = z(x_0) = a_{\text{trough}}x_0^3 + b_{\text{trough}}x_0^2 + z_{\text{gline}}. \quad (\text{A5})$$

From this point onward, the bathymetry is described by an (affine) linear function with slope s_{max} (S2,S3):

$$z(x) = z_0 + s_{\text{max}}(x - x_0). \quad (\text{A6})$$

The upper end point of this slope, (x_1, z_1) , must be chosen such that (S3) is fulfilled for the parabolic sill defined by (P3) and starting at (x_1, z_1) :

$$z(x) = \frac{a_{\text{sill}}}{2}(x - x_{\text{sill}})^2 + z_{\text{sill}}, \text{ with} \quad (\text{A7})$$

$$a_{\text{sill}} = \frac{s_{\text{max}}}{x_1 - x_{\text{sill}}}. \quad (\text{A8})$$

As eastern end point of the parabola, (x_2, z_2) , we choose the position where its slope equals $-s_{\text{max}}/2$. At this point, an exponential function with the same slope starts (S3) and decreases in accordance with (P4):

$$z(x) = a_{\text{shelf}} \exp(b_{\text{shelf}}x) + z_{\text{shelf}}, \text{ with} \quad (\text{A9})$$

$$a_{\text{shelf}} = \frac{z_2 - z_{\text{shelf}}}{\exp(b_{\text{shelf}}x_2)}, \text{ and} \quad (\text{A10})$$

$$b_{\text{shelf}} = a_{\text{sill}} \frac{x_2 - x_{\text{sill}}}{z_2 - z_{\text{shelf}}}. \quad (\text{A11})$$

In the sensitivity experiment with the sill at $z_{\text{sill}} = -400$ m (Section 3.3.4), we put the connection between parabolic sill and exponential shelf at the point where the bottom slope equals $-s_{\text{max}}/3$, to avoid $z_2 < z_{\text{shelf}}$. In the scenario without a sill, the linear slope connects directly to an exponentially increasing shelf at $z_1 = -600$ m.

A Python implementation of the here-explained mathematical expressions is provided with the model setup (Reinert, 2023b) that belongs to this paper.

A2 Model ice topography

The position of the lower ice edge is defined in our model in two parts. Between the grounding line and the calving front, we use a hyperbolic tangent shape:

$$\eta(x) = a_{\text{ice}} \tanh[b_{\text{ice}}(x - c_{\text{ice}})] + d_{\text{ice}}. \quad (\text{A12})$$

A reasonable choice of the parameters and a good fit to the ice shape near the grounding line (Fig. 1b) is obtained if the maximum ice slope is at the grounding line ($x = 0$) and has a value of $\max(d\eta/dx) = s_{\max} = 0.025$. This greatly simplifies the expression, since $c_{\text{ice}} = 0$, thus $d_{\text{ice}} = z_{\text{gline}}$, and $b_{\text{ice}} = s_{\max}/a_{\text{ice}}$. We further take $a_{\text{ice}} = 525$ m, so that the ice topography converges to $\eta = -75$ m (Fig. 1b). The Python code for the model setup (Reinert, 2023b) provided with this paper also implements the option of a maximum slope at a position c_{ice} different from the grounding line (not used in this paper), but this requires computing a_{ice} numerically to fulfill the condition that η converges to -75 m in eastward direction.

After the calving front ($x = 75$ km), we linearly connect the lower ice edge with sea level. The linear connection has a slope of 1 %, which ensures a low perturbation of the subglacial plume as it passes under the calving front (Fig. 3). With a modification of the vertical coordinates as discussed in Section 4, a higher slope might be feasible.

A3 Model stratification

Our model uses as initial and boundary conditions the same horizontally homogeneous stratification. The stratification is defined by specifying temperature and salinity at three vertical positions, with a linear interpolation of the values in between and a constant extrapolation below. In our default scenario, the salinity-values are $S(z = 0) = 29 \text{ g kg}^{-1}$, $S(z = -100 \text{ m}) = 34 \text{ g kg}^{-1}$, $S(z = -300 \text{ m}) = 35 \text{ g kg}^{-1}$ (Fig. 2a). The temperature-values are $\theta(z = 0) = -1.5 \text{ }^{\circ}\text{C}$, $\theta(z = -100 \text{ m}) = -1.0 \text{ }^{\circ}\text{C}$, $\theta(z = -300 \text{ m}) = 1.5 \text{ }^{\circ}\text{C}$ (Fig. 2b). The modified values in the sensitivity study are given in Sections 3.3.1 and 3.3.2.

Open Research

The model setup can be downloaded from <https://doi.org/10.5281/zenodo.7755753> (Reinert, 2023b) together with instructions how to reproduce the simulations presented in this paper. The corresponding GETM source code can be downloaded from <https://doi.org/10.5281/zenodo.7741925> (Klingbeil, 2023). The model output generated by this code and presented in this manuscript can be downloaded from <https://doi.org/10.5281/zenodo.7755908> (Reinert, 2023a).

This paper contains no unpublished observational data. Figure 1 uses bathymetry data published by Mayer et al. (2000) and Schaffer et al. (2019). Figure 2 shows CTD profile 115-1 from *Polarstern* cruise PS109 published by Kanzow et al. (2018).

Acknowledgments

The work of this study has been supported by the collaborative research project GROCE (Greenland Ice Sheet–Ocean Interaction) funded by the German Federal Ministry of Education and Research (BMBF, grant 03F0855E). This paper is a contribution to the projects M5 (Reducing Spurious Mixing and Energetic Inconsistencies in Realistic Ocean-Modelling Applications) and S1 (Diagnosis and Metrics in Climate Models) of the collaborative research center TRR 181 “Energy Transfers in Atmosphere and Ocean” funded by the German Research Foundation (DFG, project 274762653). ML is supported by ECAS-BALTIC funded by the German Federal Ministry of Education and Research (BMBF, grant 03F0860H). We thank Sarah Vierling (Amherst College, Massachusetts, USA) for extending the code used to create the model setup and for running many sensitivity experiments during an internship supervised by Markus Reinert in Hans Burchard’s lab, funded by the German Academic Exchange Service (DAAD) in the program “RISE Germany”. Figures in this paper use the colormaps of the cmocean package (Thyng et al., 2016).

References

- Arneborg, L., Fiekas, V., Umlauf, L., & Burchard, H. (2007). Gravity Current Dynamics and Entrainment—A Process Study Based on Observations in the Arkona Basin. *Journal of Physical Oceanography*, 37(8), 2094–2113. doi: 10.1175/JPO3110.1
- Aschwanden, A., Fahnestock, M. A., Truffer, M., Brinkerhoff, D. J., Hock, R., Khroulev, C., ... Khan, S. A. (2019). Contribution of the Greenland Ice Sheet to sea level over the next millennium. *Science Advances*, 5(6), eaav9396. doi: 10.1126/sciadv.aav9396
- Burchard, H., & Beckers, J.-M. (2004). Non-uniform adaptive vertical grids in one-dimensional numerical ocean models. *Ocean Modelling*, 6(1), 51–81. doi: 10.1016/S1463-5003(02)00060-4
- Burchard, H., & Bolding, K. (2002). *GETM – A General Estuarine Transport Model* (Tech. Rep. No. EUR 20253 EN). European Commission.
- Burchard, H., Bolding, K., Jenkins, A., Losch, M., Reinert, M., & Umlauf, L. (2022). The Vertical Structure and Entrainment of Subglacial Melt Water Plumes. *Journal of Advances in Modeling Earth Systems*, 14(3), e2021MS002925. doi: 10.1029/2021MS002925
- Burchard, H., Bolding, K., & Villarreal, M. R. (1999). *GOTM, a general ocean turbulence model: Theory, implementation and test cases*. Space Applications Institute.
- Burchard, H., & Petersen, O. (1997). Hybridization between sigma- and z-coordinates for improving the internal pressure gradient calculation in marine models with steep bottom slopes. *International Journal for Numerical Methods in Fluids*, 25(9), 1003–1023. doi: 10.1002/(SICI)1097-0363(19971115)25:9<1003::AID-FLD600>3.0.CO;2-E
- Chegini, F., Holtermann, P., Kerimoglu, O., Becker, M., Kreuz, M., Klingbeil, K., ... Burchard, H. (2020). Processes of Stratification and Destratification During An Extreme River Discharge Event in the German Bight ROFI. *Journal of Geophysical Research: Oceans*, 125(8), e2019JC015987. doi: 10.1029/2019JC015987
- Christmann, J., Helm, V., Khan, S. A., Kleiner, T., Müller, R., Morlighem, M., ... Humbert, A. (2021). Elastic deformation plays a non-negligible role in Greenland’s outlet glacier flow. *Commun Earth Environ*, 2(1), 1–12. doi: 10.1038/s43247-021-00296-3
- Goldberg, D., Holland, D. M., & Schoof, C. (2009). Grounding line movement and ice shelf buttressing in marine ice sheets. *Journal of Geophysical Research: Earth Surface*, 114(F4). doi: 10.1029/2008JF001227
- Gräwe, U., Holtermann, P., Klingbeil, K., & Burchard, H. (2015). Advantages of vertically adaptive coordinates in numerical models of stratified shelf seas. *Ocean Modelling*, 92, 56–68. doi: 10.1016/j.ocemod.2015.05.008
- Griffies, S. M., Adcroft, A., & Hallberg, R. W. (2020). A Primer on the Vertical Lagrangian-Remap Method in Ocean Models Based on Finite Volume Generalized Vertical Coordinates. *Journal of Advances in Modeling Earth Systems*, 12(10), e2019MS001954. doi: 10.1029/2019MS001954
- Gwyther, D. E., Kusahara, K., Asay-Davis, X. S., Dinniman, M. S., & Galton-Fenzi, B. K. (2020). Vertical processes and resolution impact ice shelf basal melting: A multi-model study. *Ocean Modelling*, 147, 101569. doi: 10.1016/j.ocemod.2020.101569
- Haney, R. L. (1991). On the Pressure Gradient Force over Steep Topography in Sigma Coordinate Ocean Models. *Journal of Physical Oceanography*, 21(4), 610–619. doi: 10.1175/1520-0485(1991)021<0610:OTPGFO>2.0.CO;2
- Hofmeister, R., Burchard, H., & Beckers, J.-M. (2010). Non-uniform adaptive vertical grids for 3D numerical ocean models. *Ocean Modelling*, 33(1), 70–86. doi: 10.1016/j.ocemod.2009.12.003

- 1026 Holland, D. M., & Jenkins, A. (1999). Modeling Thermodynamic Ice–Ocean Inter-
1027 actions at the Base of an Ice Shelf. *J. Phys. Oceanogr.*, 29(8), 1787–1800. doi:
1028 10.1175/1520-0485(1999)029<1787:MTIOIA>2.0.CO;2
- 1029 Holland, P. R., & Feltham, D. L. (2006). The Effects of Rotation and Ice Shelf
1030 Topography on Frazil-Laden Ice Shelf Water Plumes. *Journal of Physical*
1031 *Oceanography*, 36(12), 2312–2327. doi: 10.1175/JPO2970.1
- 1032 Horwath, M., Gutknecht, B. D., Cazenave, A., Palanisamy, H. K., Marti, F.,
1033 Marzeion, B., ... Benveniste, J. (2022). Global sea-level budget and
1034 ocean-mass budget, with a focus on advanced data products and uncer-
1035 tainty characterisation. *Earth System Science Data*, 14(2), 411–447. doi:
1036 10.5194/essd-14-411-2022
- 1037 Huang, R. X. (1993). Real Freshwater Flux as a Natural Boundary Condition for
1038 the Salinity Balance and Thermohaline Circulation Forced by Evaporation and
1039 Precipitation. *Journal of Physical Oceanography*, 23(11), 2428–2446. doi:
1040 10.1175/1520-0485(1993)023<2428:RFFAAN>2.0.CO;2
- 1041 Humbert, A., Christmann, J., Corr, H. F. J., Helm, V., Höyns, L.-S., Hofstede, C.,
1042 ... Zeising, O. (2022). On the evolution of an ice shelf melt channel at the
1043 base of Filchner Ice Shelf, from observations and viscoelastic modeling. *The*
1044 *Cryosphere*, 16(10), 4107–4139. doi: 10.5194/tc-16-4107-2022
- 1045 Inall, M. E., & Gillibrand, P. A. (2010). The physics of mid-latitude fjords: A re-
1046 view. *Geological Society, London, Special Publications*, 344(1), 17–33. doi: 10
1047 .1144/SP344.3
- 1048 IOC, SCOR, & IAPSO. (2010). The international thermodynamic equation of sea-
1049 water – 2010: Calculation and use of thermodynamic properties. *Intergovern-*
1050 *mental Oceanographic Commission, Manuals and Guides No. 56, UNESCO.*
1051 doi: 10.25607/OBP-1338
- 1052 IPCC. (2022). Summary for policymakers [Book Section]. In H. O. Pörtner et al.
1053 (Eds.), *Climate change 2022: Impacts, adaptation, and vulnerability. contribu-*
1054 *tion of working group ii to the sixth assessment report of the intergovernmental*
1055 *panel on climate change* (p. In Press). Cambridge, UK: Cambridge University
1056 Press. (In Press)
- 1057 Jenkins, A., Hellmer, H. H., & Holland, D. M. (2001). The Role of Meltwater
1058 Advection in the Formulation of Conservative Boundary Conditions at an
1059 Ice–Ocean Interface. *Journal of Physical Oceanography*, 31(1), 285–296. doi:
1060 10.1175/1520-0485(2001)031<0285:TROMAI>2.0.CO;2
- 1061 Kanzow, T., Schaffer, J., & Rohardt, G. (2018). *Physical oceanography dur-*
1062 *ing POLARSTERN cruise PS109 (ARK-XXXI/4).* PANGAEA. doi:
1063 10.1594/PANGAEA.885358
- 1064 Kappelsberger, M. T., Strößenreuther, U., Scheinert, M., Horwath, M., Groh, A.,
1065 Knöfel, C., ... Khan, S. A. (2021). Modeled and Observed Bedrock Dis-
1066 placements in North-East Greenland Using Refined Estimates of Present-Day
1067 Ice-Mass Changes and Densified GNSS Measurements. *Journal of Geophysical*
1068 *Research: Earth Surface*, 126(4), e2020JF005860. doi: 10.1029/2020JF005860
- 1069 Klingbeil, K. (2023). *Source code for the coastal ocean model GETM (glacialIce*
1070 *branch).* Zenodo. (Model code) doi: 10.5281/zenodo.7741925
- 1071 Klingbeil, K., & Burchard, H. (2013). Implementation of a direct nonhydrostatic
1072 pressure gradient discretisation into a layered ocean model. *Ocean Modelling*,
1073 65, 64–77. doi: 10.1016/j.ocemod.2013.02.002
- 1074 Klingbeil, K., Lemarié, F., Debreu, L., & Burchard, H. (2018). The numerics of hy-
1075 drostatic structured-grid coastal ocean models: State of the art and future per-
1076 spectives. *Ocean Modelling*, 125, 80–105. doi: 10.1016/j.ocemod.2018.01.007
- 1077 Klingbeil, K., Mohammadi-Aragh, M., Gräwe, U., & Burchard, H. (2014).
1078 Quantification of spurious dissipation and mixing – Discrete variance de-
1079 cay in a Finite-Volume framework. *Ocean Modelling*, 81, 49–64. doi:
1080 10.1016/j.ocemod.2014.06.001

- Li, Q., Bruggeman, J., Burchard, H., Klingbeil, K., Umlauf, L., & Bolding, K. (2021). Integrating CVMix into GOTM (v6.0): A consistent framework for testing, comparing, and applying ocean mixing schemes. *Geoscientific Model Development*, 14(7), 4261–4282. doi: 10.5194/gmd-14-4261-2021
- Lindeman, M. R., Straneo, F., Wilson, N. J., Toole, J. M., Krishfield, R. A., Beaird, N. L., ... Schaffer, J. (2020). Ocean Circulation and Variability Beneath Nioghalvfjærdsbræ (79 North Glacier) Ice Tongue. *Journal of Geophysical Research: Oceans*, 125(8), e2020JC016091. doi: 10.1029/2020JC016091
- Losch, M. (2008). Modeling ice shelf cavities in a z coordinate ocean general circulation model. *Journal of Geophysical Research: Oceans*, 113(C8). doi: 10.1029/2007JC004368
- Mayer, C., Reeh, N., Jung-Rothenhäusler, F., Huybrechts, P., & Oerter, H. (2000). The subglacial cavity and implied dynamics under Nioghalvfjærdsfjorden Glacier, NE-Greenland. *Geophysical Research Letters*, 27(15), 2289–2292. doi: 10.1029/2000GL011514
- Muilwijk, M., Straneo, F., Slater, D. A., Smedsrud, L. H., Holte, J., Wood, M., ... Harden, B. (2022). Export of Ice Sheet Meltwater from Upernavik Fjord, West Greenland. *Journal of Physical Oceanography*, 52(3), 363–382. doi: 10.1175/JPO-D-21-0084.1
- Reinert, M. (2023a). *Output files of the 2DV-model for the 79NG fjord*. Zenodo. (Dataset) doi: 10.5281/zenodo.7755908
- Reinert, M. (2023b). *Setup files of the 2DV-model for the 79NG fjord*. Zenodo. (Model setup) doi: 10.5281/zenodo.7755753
- Rignot, E., & Steffen, K. (2008). Channelized bottom melting and stability of floating ice shelves. *Geophysical Research Letters*, 35(2). doi: 10.1029/2007GL031765
- Schaffer, J., Kanzow, T., von Appen, W.-J., von Albedyll, L., Arndt, J. E., & Roberts, D. H. (2020). Bathymetry constrains ocean heat supply to Greenland’s largest glacier tongue. *Nature Geoscience*, 13(3), 227–231. doi: 10.1038/s41561-019-0529-x
- Schaffer, J., Timmermann, R., Arndt, J. E., Rosier, S. H. R., Anker, P. G. D., Callard, S. L., ... Roberts, D. H. (2019). *An update to Greenland and Antarctic ice sheet topography, cavity geometry, and global bathymetry (RTopo-2.0.4)*. PANGAEA. doi: 10.1594/PANGAEA.905295
- Schaffer, J., von Appen, W.-J., Dodd, P. A., Hofstede, C., Mayer, C., de Steur, L., & Kanzow, T. (2017). Warm water pathways toward Nioghalvfjærdsfjorden Glacier, Northeast Greenland. *Journal of Geophysical Research: Oceans*, 122(5), 4004–4020. doi: 10.1002/2016JC012462
- Shepherd, A., Wingham, D., & Rignot, E. (2004). Warm ocean is eroding West Antarctic Ice Sheet. *Geophysical Research Letters*, 31(23). doi: 10.1029/2004GL021106
- Stolzenberger, S., Rietbroek, R., Wekerle, C., Uebbing, B., & Kusche, J. (2022). Simulated Signatures of Greenland Melting in the North Atlantic: A Model Comparison With Argo Floats, Satellite Observations, and Ocean Reanalysis. *Journal of Geophysical Research: Oceans*, 127(11), e2022JC018528. doi: 10.1029/2022JC018528
- Straneo, F., & Cenedese, C. (2015). The Dynamics of Greenland’s Glacial Fjords and Their Role in Climate. *Annu. Rev. Mar. Sci.*, 7(1), 89–112. doi: 10.1146/annurev-marine-010213-135133
- Thyng, K. M., Greene, C. A., Hetland, R. D., Zimmerle, H. M., & DiMarco, S. F. (2016). True Colors of Oceanography: Guidelines for Effective and Accurate Colormap Selection. *Oceanography*, 29(3), 9–13.
- Timmermann, R., Wang, Q., & Hellmer, H. H. (2012/ed). Ice-shelf basal melting in a global finite-element sea-ice/ice-shelf/ocean model. *Annals of Glaciology*, 53(60), 303–314. doi: 10.3189/2012AoG60A156

- 1136 Umlauf, L., Arneborg, L., Hofmeister, R., & Burchard, H. (2010). Entrainment
1137 in Shallow Rotating Gravity Currents: A Modeling Study. *Journal of Physical*
1138 *Oceanography*, *40*(8), 1819–1834. doi: 10.1175/2010JPO4367.1
- 1139 Umlauf, L., & Burchard, H. (2005). Second-order turbulence closure models for geo-
1140 physical boundary layers. A review of recent work. *Continental Shelf Research*,
1141 *25*(7), 795–827. doi: 10.1016/j.csr.2004.08.004
- 1142 Vallis, G. K. (1992). Mechanisms and Parameterizations of Geostrophic Adjustment
1143 and a Variational Approach to Balanced Flow. *Journal of the Atmospheric Sci-*
1144 *ences*, *49*(13), 1144–1160. doi: 10.1175/1520-0469(1992)049<1144:MAPOGA>2
1145 .0.CO;2